The Thesis committee for Yihua Cai
certifies that this is the approved version of the following thesis:

Spectral Recomposition and Multicomponent Seismic Image Registration

APPROVED BY

SUPERVISING COMMITTEE:

Sergey B. Fomel, Supervisor

Bob A. Hardage

Clark R. Wilson

Spectral Recomposition and Multicomponent Seismic Image Registration

by

Yihua Cai, B.Phr.; M.Phr.; M.S.Stat.

THESIS

Presented to the Faculty of the Graduate School of

The University of Texas at Austin

in Partial Fulfillment

of the Requirements

for the Degree of

MASTER OF SCIENCE IN GEOLOGICAL SCIENCES

THE UNIVERSITY OF TEXAS AT AUSTIN

May 2012

Dedicated to my parents.

Acknowledgments

It is difficult to overstate my gratitude to my supervisor, Dr.Sergey Fomel. His perpetual energy and enthusiasm in research has motivated all his advisees, including me. His guidance and inspiration makes my geophysics study and research easier. I feel very grateful to Dr.Bob Hardage and Dr.Clark Wilson who gave me lots of very good suggestions on writing this thesis. My wife Xiaoyan Jiang has been, always, my pillar, my joy and my guiding light, and I thank her.

I would also like to thank Dr.Stephen Grand, Dr.Peter Flemings, Dr.Ronald Steel, Philip Guerrero, Jennifer Logan, Karl Schleicher. Within our group (now the Texas Consortium for Computational Seismology—TCCS), I would like to thank William Burnett, Vladimir Bashkardin, Yang Liu, Jules Browaeys, Hesam Kazemeini, Alexander Klokov, Roman Kazinnik, Jingwei Hu, Siwei Li, Xiaolei Song, Jiubing Chen, Parvaneh Karimi, Shaunak Ghosh, and Salah Alhadab. I thank TCCS sponsors for funding my research.

Lastly, and most importantly, I wish to thank my parents, Haishan Wang and Guanming Cai. They bore me, raised me, supported me, taught me. To them I dedicate this thesis.

Spectral Recomposition and Multicomponent Seismic Image Registration

Yihua Cai, M.S.Geo.Sci.

The University of Texas at Austin, 2012

Supervisor: Sergey B. Fomel

Spectral recomposition splits a seismic spectrum into Ricker components. It provides a tool for imaging and mapping temporal bed thicknesses and geologic discontinuities. I propose an application of separable, nonlinear, least-squares estimation in spectral recomposition. Employing the Gauss-Newton method, this approach estimates fundamental signal parameters such as peak frequencies and amplitudes. I applied spectral recomposition to multicomponent seismic data, which provides new perspectives of seismic attributes and multicomponent data interpretation. Correlating S-wave reflection with P-wave reflection is one of the very first steps in multicomponent data interpretation. In a given stratigraphic interval of a geologic section, registration correlates P and S-wave profiles to determine t_s/t_p ratios, which are equivalent to V_p/V_s ratios for vertical propagation paths. The registration process is largely driven by the availability of dipole sonic logs. However, dipole sonic logs are not as common as standard sonic logs and tend to be affected by various borehole factors. Therefore, new techniques are needed for accurate PP and PS correlation and registration. Assuming PP and PS reflection events have been correctly positioned laterally in migrated images, and the difference between PP wave image and PS wave image can be explained only by vertical

transformation, I adopt a multistep approach to register PP and PS images automatically. Setting PP time as a coordinate system, I was able to squeeze PS traces accordingly while keeping the signal pattern of PS wave data. Local seismic attributes, such as the local similarity, help improve registration accuracy.

Table of Contents

List of Tables

List of Figures

Chapter 1

Introduction

Rapid advancements in both land and marine multicomponent seismic data acquisition and processing have lead to numerous applications of converted wave data in exploration and production. Multicomponent seismic data have been increasingly used in structural imaging, lithology estimation, anisotropy analysis, subsurface fluid description, and reservoir monitoring (Stewart et al., 2003). However, from the interpreter's point of view, multicomponent data present numerous difficulties and uncertainties (Cary, 2001). Most interpretation packages used in the industry do not work well for multicomponent data imaging and interpretation. The registration of PP and PS data remains a topic of concern among interpreters, as well as a focus of technology development (DeAngelo et al., 2003).

Different methods have been proposed and developed for multicomponent seismic image registration. Tatham et al. (1991) discussed using faulting, overall structural character and stratigraphic sequence boundaries in P and S wave correlation. If available, borehole logging and vertical seismic profile (VSP) data provide more reliable information (DeAngelo et al., 2003). Hardage et al. (2011) describe the recent development in depth registration methods, such as using VSP data, V_p and V_s velocities, thin-bed stratigraphy etc.

Several numerical methods have been developed to automate the process of multicomponent image registration, including an algorithm for pairwise alignment of seismic traces (Liner and Clapp, 2004) and a least-squares optimization (Fomel and Backus, 2003; Nickel and Sonneland, 2004). How-

ever, unless the images are properly preprocessed to minimize the inevitable differences in amplitude and frequency content, these automatic approaches will fail (Fomel et al., 2005). Fomel and Backus (2003) and Fomel et al. (2005) developed a multistep approach that takes all the differences into consideration while automatically extracting a high-resolution mapping of PS reflection events to the corresponding PP times.

Frequency domain seismic data attributes are important in data processing and interpretation (Castagna et al., 2003; Li et al., 2011). Spectral decomposition has been used in interpretation because it can help capture seismic response at each frequency subset. Various time-frequency analysis methods have been employed for frequency decomposition. Some researchers applied short-time Fourier transforms (Dilay and Eastwood, 1995; Partyka et al., 1999), which suffers from a time-frequency resolution limit (Chakraborty and Okaya, 1995). Liu (2006) and Chen et al. (2008) applied spectral decomposition in the time domain by decomposing the seismogram into constituent wavelets, and then summing the Fourier spectra of individual wavelets. This approach experiences difficulties when the frequency range is large, and it relies on the accuracy of wavelet decomposition, whose residuals commonly introduce bias into "frequency gathers."

I propose spectral recomposition using separable, nonlinear, least-squares estimation. Tomasso et al. (2010) defined frequency recomposition in seismic forward modeling as estimations of Ricker components of the seismic spectrum by manual picking of component frequencies and amplitudes, which is not accurate and depends on personal skill and experience. Spectral recomposition using nonlinear least-squares estimation simultaneously and automatically fits both linear and nonlinear parts of the Ricker wavelet spectrum. The method provides an accurate and direct estimation of amplitudes and peak frequencies of various Ricker wavelets. Using separable, nonlinear, least-squares estimation, spectral recomposition estimates individual frequency components, and provides detailed

information about the subsurface frequency response. I used the Gauss-Newton algorithm, a method of minimizing the residual sum of squares. It is effective both when residuals are small and when measurement errors are additive and the data set is large (Osborne, 2007).

I analyzed multicomponent seismic data with separable nonlinear least-squares estimation, and then applied the multistep approach of multicomponent seismic image registration on field data.

To summarize my contribution, I have proposed spectral recomposition using separable nonlinear least-squares estimation. Applying spectral recomposition analysis on field data, I was able to improve seismic images for both vertical and horizontal slices. Using spectral recomposition, I analyzed multicomponent seismic data attributes, and applied a multistep approach for multicomponent seismic image registration. The registration result shows PP-wave image and PS-wave image matching each other.

This thesis is divided into six parts:

- Chapter 1: Introduction including background information,
- Chapter 2: Review of multicomponent seismology,
- Chapter 3: Spectral recomposition using nonlinear least-squares estimation and its application,
- Chapter 4: A multistep approach to multicomponent seismic image registration,
- Chapter 5: Conclusions,
- Appendix: C code and Madagascar scripts.

Chapter 2

Review of Multicomponent Seismology

Multicomponent Seismic Exploration

In exploration seismology, two different body waves are generated. One is labeled primary or P wave, with a particle displacement parallel to the direction of wave propagation. The other wave is secondary, or S wave, with a particle displacement perpendicular to the direction of wave propagation, as shown in Figure 2.1. With passage of the P-wave, due to alternating compressive and tensional stresses, the rock changes volume but not shape. With the passage of the S-wave, the rock changes shape but not volume (Aki and Richards, 2009).

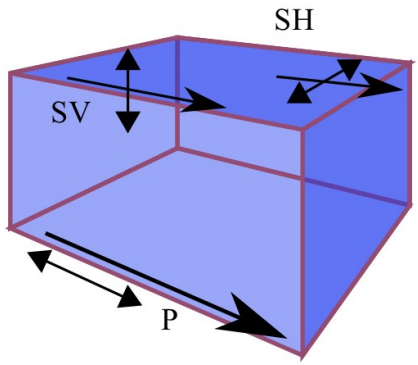

Figure 2.1: For P-wave, particles move along the direction of P-wave propagation. For SV-wave and SH-wave, particles move perpendicularly to the direction of wave propagation. chapter2/data cube2

Using both P-waves and S-waves, multicomponent exploration, which helps collect more

information than conventional exploration, has come a long way in the past three or four decades. Multicomponent seismic technology has been used in exploration and production since the 1970s (Stewart et al., 2002). Geophysical activity for S-wave acquisition has been reported by the SEG Geophysical Activities Committee as early as 1980 (Tatham et al., 1991). S-wave studies have been carried out through the history of exploration seismology. One of the earliest recording of using S-wave in exploration application was reported by Horton (1943). More and more exploration companies have become involved in multicomponent seismic exploration since then. According to Tatham et al. (1991), following Conoco Shear-Wave Group, about a half-dozen companies began to operate S-wave land crews in the early 1980s because of the encouraging results.

Resolution describes the minimum distance between two impedance boundaries represented by two events on a single trace in which both events remain distinctive and measurable. The imaging process assigns events recorded on a set of seismic traces to proper physical locations. Resolution of seismic images depends on the method and accuracy of the imaging algorithm, the set of seismic traces chosen to derive an image, and temporal-frequency content captured in the seismic traces (Meier and Lee, 2009). S-wave velocity is significantly lower than P-wave, and the frequency of S-wave is initially fairly close to the frequency of P-wave. Because S-wave has a shorter wavelength than a P-wave, processors and interpreters may expect S-wave data to improve image resolution. When properly processed, PP and PS images made from multicomponent seismic data acquired in deepwater with seafloor sensors show near-seafloor geology with impressive detail and high resolution (Backus et al., 2006a). However, S-wave energy is attenuated much faster compared with P-wave energy (Browaeys and Fomel, 2009). In addition, generating pure S-wave for exploration purposes gives rise to difficulties in exploration practice.

A converted-wave is seismic energy that has traveled partly as a P-wave and partly as an S-

wave, being converted from one to the other upon reflection or refraction at oblique incidence on an interface (Sheriff, 2002). Combining P-wave and S-wave information, multicomponent seismology provides us a better solution for various resources exploration.

At some oil-saturated sandstone boundaries, both bulk density and P-wave velocity are relatively small, and the impedance contrast is relatively small, hence the energy of P-wave reflectivity is weak. However, S-wave reflectivity is often strong in these cases. With the help of converted modes, we might be able to detect and image such reservoir boundaries accurately. Moreover, converted-wave data usually provide better images of reservoirs underneath a gas cloud. Passing through a gas-bearing sediment, P-wave energy is scattered and attenuated. Leaky gas reservoirs create a gas plume or chimney, which makes P-wave imaging difficult. Being generally less sensitive to rock saturants, S-waves can be used to penetrate gas-saturated sediments. Rodriguez (2000) and Stewart et al. (2003) provide a four-component (4C) case of using prestack equivalent-offset migration for converted waves to image through a gas cloud. The storage of oil or gas and a reservoir's producibility can depend on the fracture state of the reservoir. Fractures have great influence on reservoir porosity and permeability. Converted-wave seismic data provide complementary surface seismic information to help identify fracture properties, such as fracture density and orientation (Li, 1998). It has been shown that PS-waves have potential impact on geological and petrophysical description of fractured reservoirs using both land and marine data (Gaiser et al., 2001; van Dok et al., 2001). Moreover, repeating 3-D multicomponent survey allows for time-lapse (4-D) imaging. As the pressure and saturation state of a reservoir is altered in the course of hydrocarbon production, the elastic (as well as acoustic) properties of the rock change, demonstrating the need for full (3C-4D or 4C-4D) multicomponent recording and analysis.

In summary, the applications and potential applications of converted wave data are (Cald-

well, 1999; Gaiser, 1999; Zhu et al., 1999; Yilmaz, 2001; Hardage et al., 2011)

- imaging beneath gas plumes,
- imaging beneath salt domes,
- imaging beneath basalts,
- delineating reservoir boundaries with a higher S-wave impedance contrast than P-wave impedance contrast,
- differentiating sand from shale,
- detection of fluid phase change from oil-bearing to water-bearing sands,
- detection of vertical fracture orientation,
- mapping hydrocarbon saturation, and
- mapping oil-water contact.

Mode Conversion

Acoustic wave propagation involves reflection, refraction and transmission of wave fronts, hence seismic reflection imaging can be defined in purely geometrical terms as a transformation of reflection travel time surfaces in the data to reflector surfaces in an image of the Earth interior. However, in the elastic case, it becomes more complicated. We have not only reflection and refraction, but also mode conversion, as shown in Figure 2.3.

Elastic wave modes are usually designated as P-P, SH-SH, SV-SV, P-SV and SV-P. The SH mode is considered a simpler S-wave mode than SV, because there is no energy transfer between

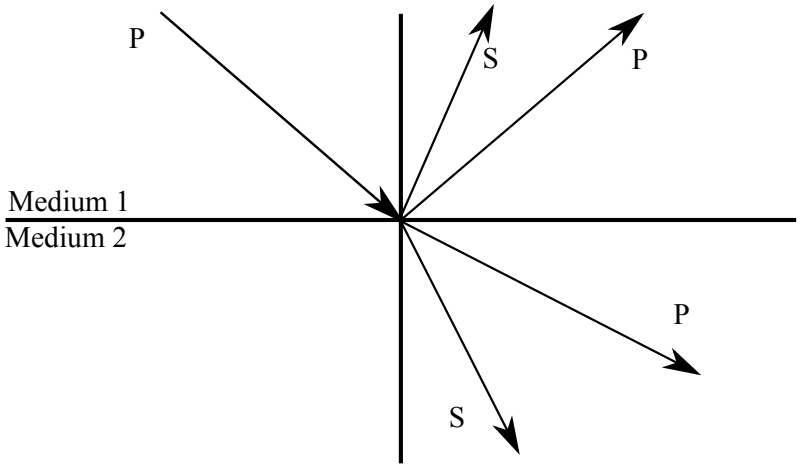

Figure 2.2: At the boundary, part of the P-wave energy reflects and refracts as P-wave energy, and part of the P-wave energy converts to SV-wave energy. chapter2/data mode

SH and P modes or between SH and SV modes at reflecting interfaces. Mode conversion means a P-wave converts to an SV-wave or an SV-wave converts to a P-wave. Figure 2.3 shows examples of synthetic PP-wave data and PS-wave data reflected from the same flat reflector. Figure 2.4 and Figure 2.5 show the model and synthetic data of multicomponent data. The model and the synthetic data include the sealing, reservoir and top of salt.

Instead of a pure P-P mode, we could have P-SV-SV-P for two layers of reflectors. As a matter of fact, geophysicists did not recognize they finally had access to a source that could generate an SH shear mode until the horizontal vibrator was introduced (Tatham et al., 1991). [1] It turns

[1]Consider a source consisting of a base-plate pressed against the ground on the zero position of a seismic line trending North. A hammer blow against the eastern face of the base-plate generates P and S-waves starting with a northwest displacement while a blow against the western face generates waves starting with a northeast displacement. In the subtraction of the two records, we have pure SH-wave components (Danbom and Domenico, 1987).

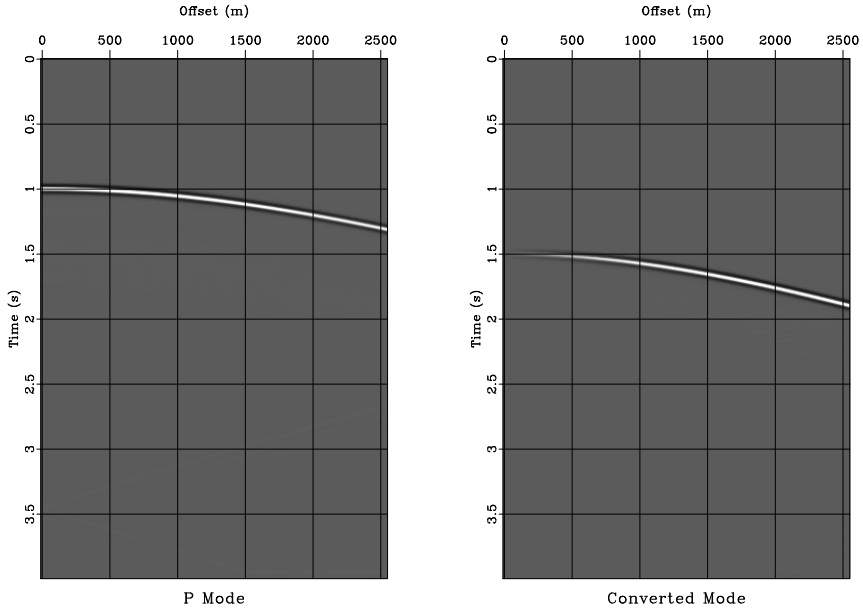

Figure 2.3: Synthetic data of P-P mode and P-SV mode from the same flat reflector. The converted mode has slower velocity. chapter2/onelayer mode

out that nine-component seismic data contains all the wave modes. That is, at the source location, three orthogonal source displacement vectors are generated, for each of which three orthogonal vector sensors record the wave fields. For isotropic media, in the case of a one-layer reflector, we have four different waves involved:

- reflected P-wave,
- reflected mode converted SV-wave,
- transmitted/refracted P-wave, and
- transmitted/refracted SV-wave.

The common presence of fractured rocks and tectonic-stressed rocks makes S-wave propa-

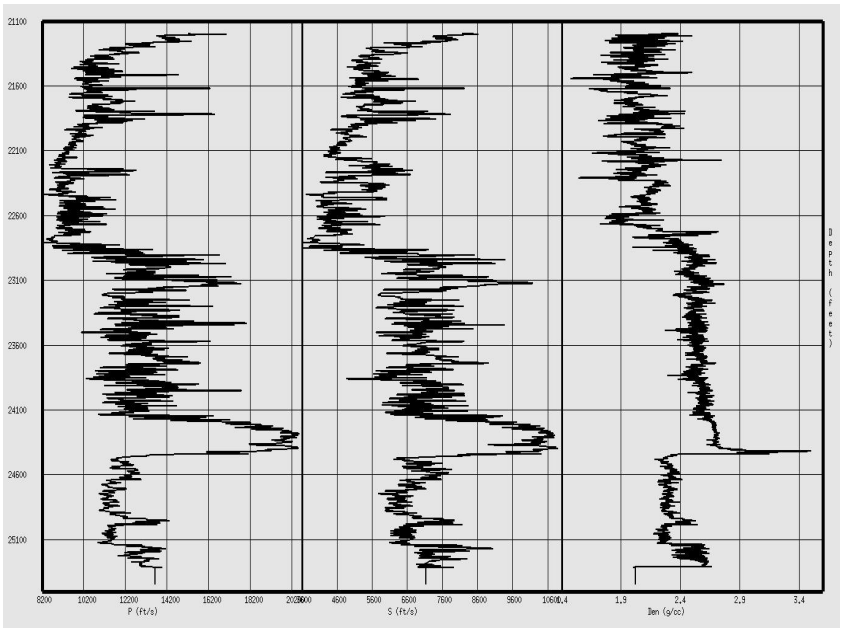

Figure 2.4: The model used to generate synthetic seismic data includes V_p, V_s and density. chapter2/marine model

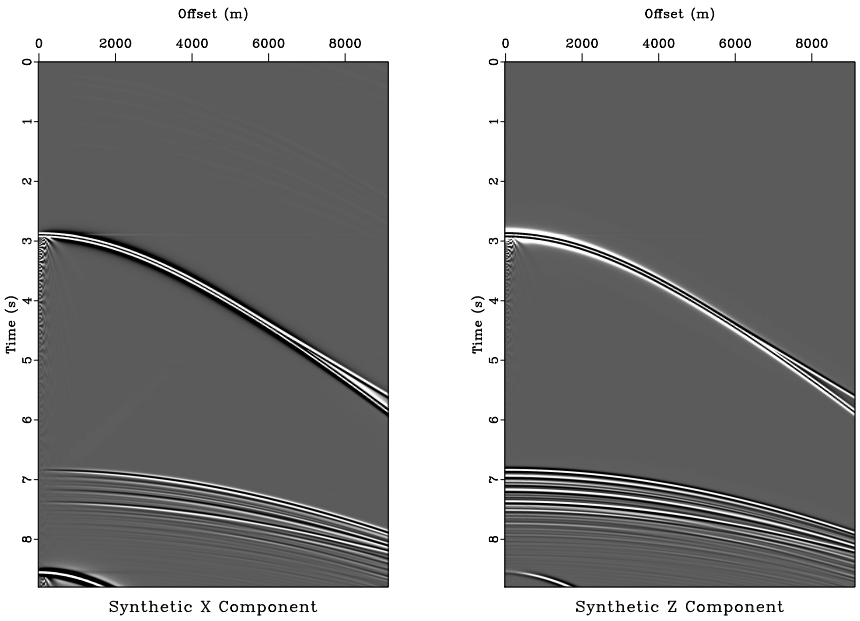

Figure 2.5: X (inline) and Z (vertical) components of synthetic data with direct wave removed. chapter2/marine shotgather

gation in anisotropic media important. Recently, increasing exploration and production of shale gas brings more and more attention to this topic. Due to vertical fractures or significant differences between maximum and minimum horizontal stress vectors throughout the overburden above a seismic target, a shear wave traveling in an anisotropic media splits into a fast-S mode and a slow-S mode that have orthogonal displacement vectors (Hardage et al., 2011). In anisotropic media, the P-wave is not polarized in either the slowness or ray directions; similarly, the SV-wave in anisotropic media is not polarized normal to the slowness and ray directions. That is, in anisotropic media, instead of pure P, SV and SH modes, there are quasi-P wave, quasi-SV wave etc (Tsvankin and Grechka, 2011).

Mode separation is important because amplitude-versus-offset responses of different modes are different, e.g. the AVO responses of SH and SV reflections are different in both isotropic and anisotropic media. Different modes can be separated by the transformation to radial-transverse coordinates because the field coordinates implicitly record a mixture of quasi-SV and quasi-P waves (Simmons and Backus, 2001).

Elasticity and Converted Waves

Exploration seismology involves analysis of straining or internal deformation. Stress is the intensity of force acting on a body, in terms of force per unit area: stress = stiffness tensor $\times$ strain. A stress tensor is made up of nine components, which combine to keep a solid volume in equilibrium, and can be written as,

$$\mathbf{P} = \begin{bmatrix} P_{xx} & P_{xy} & P_{xz} \\ P_{yx} & P_{yy} & P_{yz} \\ P_{zx} & P_{zy} & P_{zz} \end{bmatrix} , \tag{2.1}$$

where the diagonal elements are the normal stress components and the off-diagonal elements are the shear stress components.

Strain is the change of dimensions or shape produced by a stress. Strain is usually expressed in dimensionless units such as change of length per unit of length. If u, v, w are the stresses produced by displacements in the x, y, z directions of a point in an anisotropic body, the normal strains are,

$$\epsilon_{xx} = \frac{\partial u}{\partial x} \, , \epsilon_{yy} = \frac{\partial v}{\partial y} \, , \epsilon_{zz} = \frac{\partial w}{\partial z} \, ; \tag{2.2}$$

and the shearing strains are,

$$\epsilon_{xy} = \epsilon_{yx} = \frac{\partial v}{\partial x} + \frac{\partial u}{\partial y} \, , \epsilon_{yz} = \epsilon_{zy} = \frac{\partial w}{\partial y} + \frac{\partial v}{\partial z} \, , \epsilon_{zx} = \epsilon_{xz} = \frac{\partial u}{\partial z} + \frac{\partial w}{\partial x} \, . \tag{2.3}$$

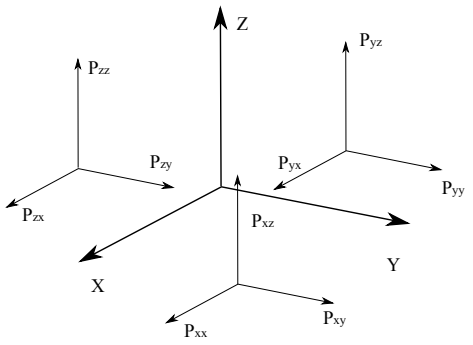

Figure 2.6: Stress components in a Cartesian coordinate system. chapter2/data2 stress

For a displacement component u, according to Newton's second law of motion, we have

$$\rho \frac{\partial^2 u}{\partial t^2} = \frac{\partial P_{xx}}{\partial x} + \frac{\partial P_{xy}}{\partial y} + \frac{\partial P_{xz}}{\partial z} \tag{2.4}$$

where ρ is the density. The stress components in a Cartesian coordinate system have been plotted in Figure 2.6. Applying Hooke's law in an isotropic medium, we can derive the equation of wave propogation (Aki and Richards, 2009)

$$\rho \frac{\partial^2 \boldsymbol{u}}{\partial t^2} = (\lambda + \mu) \Delta \nabla + \mu \nabla^2 \boldsymbol{u} \, , \tag{2.5}$$

where $\boldsymbol{u}(u, v, w)$ is the displacement factor, ρ is the density, λ and μ are Lamé parameters. Equation 2.5 can be used to describe various wave types within solids and fluids. Thus, we are able to derive the equations of both P-wave and S-wave propogation. The equation for P-wave propogation is:

$$\rho \frac{\partial^2 \boldsymbol{u}}{\partial t^2} = (\lambda + 2\mu)\nabla^2 \boldsymbol{u} \tag{2.6}$$

The velocity of P-wave propogation in an elastic solid is

$$V_p = \sqrt{\frac{\lambda + 2\mu}{\rho}} \tag{2.7}$$

The S-wave propogation equation is

$$\rho \frac{\partial^2 \boldsymbol{\Theta}}{\partial t^2} = \mu \nabla^2 \boldsymbol{\Theta} \,, \tag{2.8}$$

where $\boldsymbol{\Theta}$ is the rotational vector. The velocity of S-wave propagates in an elastic solid is

$$V_s = \sqrt{\frac{\mu}{\rho}} \,. \tag{2.9}$$

Multicomponent Data Character

Three-component geophones are the oldest and most common type of vector sensors used to acquire multicomponent seismic data across onshore seismic prospects. Recently, microelectromechanical system (MEMS) devices have been used in land multicomponent data acquisition. Land data acquisition is based partly on tradition and partly on seismic data processing requirements (Yilmaz, 2001). For ocean bottom surveys, two sensor systems are employed: a node system or a cable system. In a cable system, marine 4-C data are recorded using ocean-bottom cables with receiver units, that contain one hydrophone to detect the pressure wavefield and three geophones to detect particle motions in a Cartesian system. Usually a cable several kilometers long with multicomponent sensor packages positioned at short intervals of a few meters is deployed on the seafloor.

The sensor package itself is a combination of hydrophones and 3C geophones or a combination of hydrophones and MEMS sensors (Hardage et al., 2011). The vertical geophone measures the vertical component of the particle motion. The two horizontal components measure the particle motions in two orthogonal directions, and one of them is aligned in the direction of the receiver cable. The vertical z-component is positive downward, the inline x-component is defined to have positive direction, the crossline y-component is clockwise with respect to the x-component. Acquiring multicomponent marine data with ocean-bottom-sensor (OBS) nodes is preferred when water depth exceeds 1000 m (Hardage et al., 2011). In OBS surveys, each individual node holds a hydrophone and three geophones in the Cartesian orientation, and the node is deployed in the seabed sediments by a remotely operated vehicle.

Tables 2.1 and 2.2 reiterate the concept of multicomponent seismic acquisition and recording. Mnemonics used to indicate terms are, for vertical (P), horizontal in-line (SV) and horizontal transverse (SH) orientations of sources and receivers relative to the seismic survey line. SV_1 and SH_1 are fast shear waves, SV_2 and SH_2 are slow shear waves. Conceptually, processing pure S-wave data of isotropic media is no different than processing conventional P-wave data, e.g. SV-SV and SH-SH in table 2.1. In exploration practice, P-SV converted wave is widely used, especially in marine exploration, due to the high cost of shear-wave excitation and difficulty of placing shear wave sources on sear floor in marine data acquisition.

Although we see subtle similarities of seismic events between PP-wave and SS-wave images in Figure 2.7 and Figure 2.8, the difference between them are apparent. It is difficult for us to correlate the SS-wave image with the PP-wave image without using any tools. PP-wave and SS-wave data almost always differ in parameters such as signal-to-noise ratio and bandwidth despite our efforts to equalize them. In addition, "leakage" of signals and noises between components also

Table 2.1: Data acquisition, recording options and seismic modes in isotropic media (Hardage et al., 2011)

Acquisition option	Source	Receiver	Captured mode
1C	Z	Z	P-P
3C	Z	XYZ	P-P, P-SV
4C	Z or A	XYZH	P-P, P-SV
6C	YZ	ZYZ	P-P, P-SV, SH-SH
9C	XYZ	XYZ	P-P, P-SV, SV-SV, SV-P, SH-SH

Table 2.2: Data acquisition, recording options and seismic modes in anisotropic media (Hardage et al., 2011)

Acquisition option	Source	Receiver	Captured mode
1C	Z	Z	P-P
3C	Z	XYZ	P-P, P-SV_1, P-SV_2
4C	Z or A	XYZH	P-P, P-SV_1, P-SV_2
6C	YZ	ZYZ	P-P, P-SV_1, P-SV_2, SH_1-SH_1, SH_2-SH_2
9C	XYZ	XYZ	P-P, P-SV_1, P-SV_2, SV_1-SV_1, SV_2-SV_2, SV_1-P, SV_2-P, SH_1-SH_1, SH_2-SH_2

gives rise to difficulties in processing. Leakage can occur because P-wave energy could be recorded on the S-wave components due to the non-vertical arrival of P ray paths at a sensor station. If the vector properties of certain wave modes vary in unknown ways, even with the help of advanced processing algorithms and techniques, people may not be able to retrieve solid information from the acquired data (Hardage et al., 2011).

It is expected that S-waves would yield better resolution than P-waves if the frequency content were the same. Backus et al. (2006b) have shown multicomponent seismic data has unique value in studying near-seafloor geology in deepwater environments. However, in terms of resolution, S-wave recording has no advantage over conventional P-wave recording, because attenuation

of higher frequencies limited wavelengths of S-waves roughly to those of P-waves and frequency bandwidths to almost one-half (Tatham et al., 1991). The dominant frequency of the PS-wave data is typically about 20 to 25 Hz, whereas the dominant frequency of PP-wave data is 30 to 40 Hz.

As can be seen in Figure 2.9, the component frequencies of PP-wave spectrum are higher. Using separable nonlinear least-square estimation, PP and PS-wave trace spectral recomposition indicates that the PP-wave has more high-frequency components. The technique of spectral recomposition is introduced and explained in Chapter 3. The intensity of scattering attenuation and the value of frequency cutoff depend strongly on the size of the heterogeneities, and S-waves are more attenuated than P-waves at the same frequency (Browaeys and Fomel, 2009). Since PS data have reduced high frequency content, in many cases the resolution of the converted wave data ends up being one-half to two-thirds as good as that of PP data.

PP-wave and PS-wave Traveltimes in Data Processing

Multicomponent data registration helps identify corresponding seismic events of different modes at the same time depth. In addition to differences in component frequencies and amplitudes, differences in traveltime of various modes gives rise to difficulties in multicomponent data registration. Learning how to deal with traveltime-related topics in data processing helps us improve depth registration techniques.

Compared with PP-wave data, undesirable properties and characters of mode-converted data add difficulties in processing multicomponent data. Geophones at 3-C geophone stations are designed to record signals of different wave components. In reality, because of signals of various modes of both P and S-waves are recorded on almost all geophones, due to mode leakage. Other difficulties include asymmetric PS imaging in positive and negative offsets, polarity reversal, and

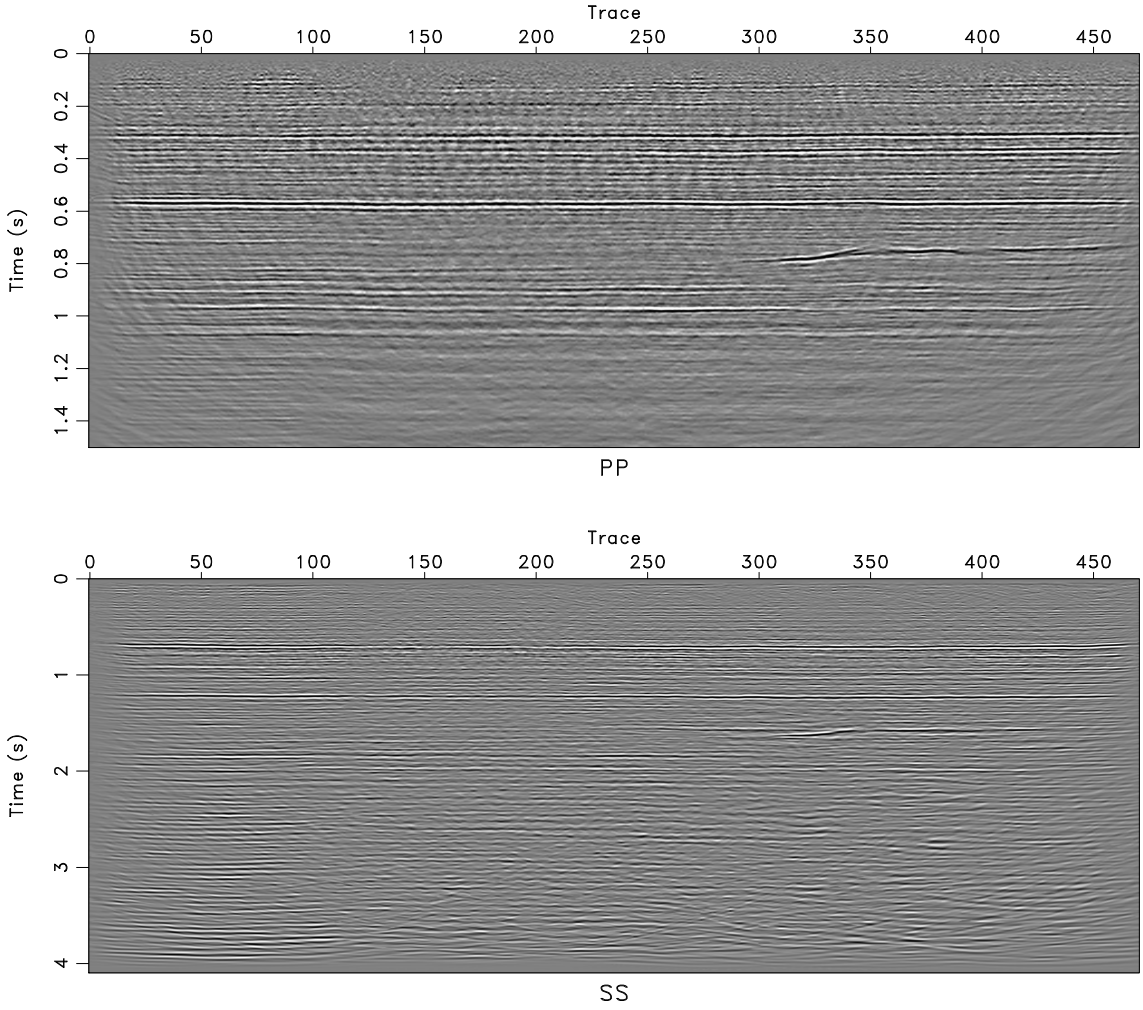

Figure 2.7: PP and SS-wave images of the same geological subsurface region. chapter2/vecta ppss

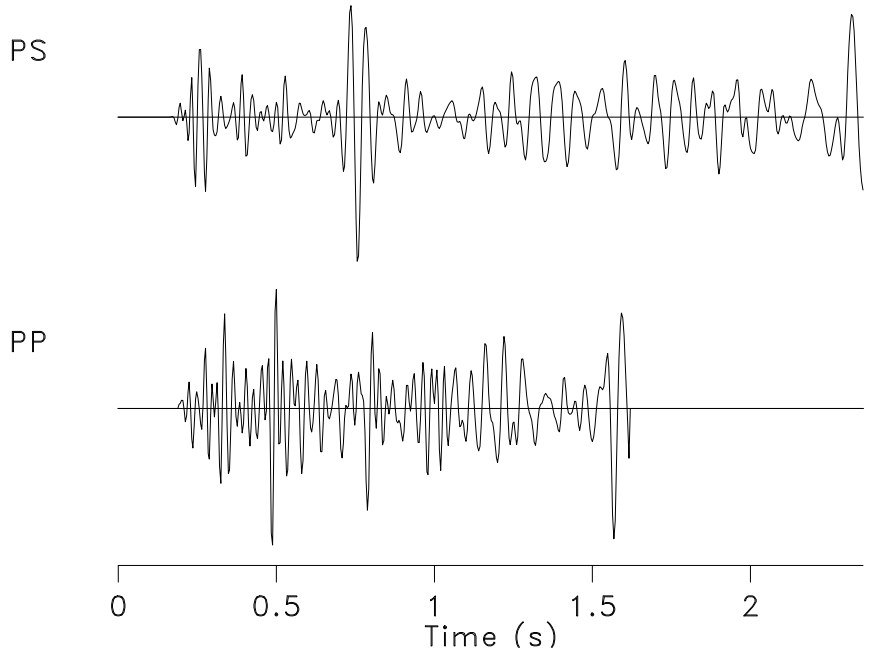

Figure 2.8: PS and PP traces at the same offset. Although the difference between these PS and PP traces is large, a few similarities in seismic events can be identified, which might help with initial registration, e.g. the event at 0.5 second in the PP trace looks similar to the event at 0.75 second in PS trace. chapter2/data2 data

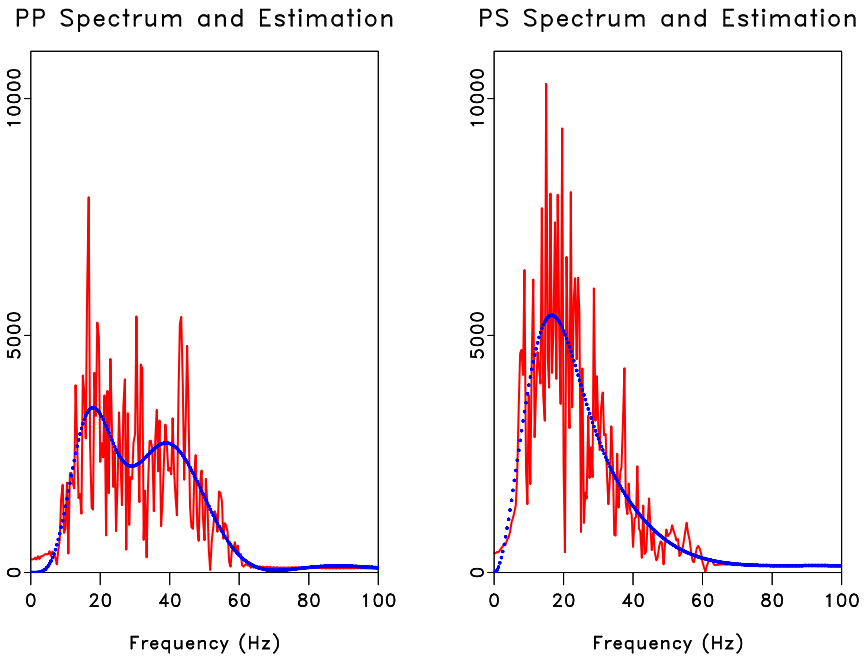

Figure 2.9: Using spectral recomposition, we estimated the spectra of both PP and PS traces. The computed spectra of PP and PS traces are plotted in solid lines. The corresponding estimations are plotted in dashed lines. chapter2/data2 spec

reflection-point dispersal.

The essential value of multicomponent data derives from the comparison of reflection arrival times and amplitudes of different components, which increases the difficulty of multicomponent data processing, because different components need to be processed in a mutually compatible way. Seismic interpretation is based on reliable processed results, thus observed differences in waveform character among any wave components should not be the result of mismatched processing parameters. Some authors even argued that the increase in processing complexity is greater than the nine-fold increase in data volume may suggest (Tatham et al., 1991).

CMP and CCP Processing

Converted-mode processing is different from P-P mode data processing. For converted modes, such as P-SV and SV-P modes, the image point does not occur at a common-midpoint coordinate as in CMP imaging. Instead, it occurs at a common-conversion-point, because the velocity of the downgoing wavefield is different from the velocity of the upgoing wavefield (Tatham et al., 1991).

A premise of common-midpoint processing is the downgoing propagation velocity is the same as the upgoing propagation velocity. Such a premise is no longer valid for mode-converted seismic data, which is probably the most common S-wave data we have. The downgoing propagation velocity (P) is no longer the same as the upgoing propagation velocity (SV), therefore the downgoing and upgoing travel path are no longer symmetric. As a direct result, the notion of a CMP gather based on sorting PP-data from acquisition coordinates source and receiver is not applicable to PS-data. Instead, PS-data need to be sorted into common conversion point (CCP) gathers, such that traces of a single CCP gather have the same conversion point coordinate.

The fact that different velocity behavior is observed in opposite offset directions for P-SV and SV-P imaging is a fundamental distinction between the wave physics of CMP and CCP seismic data. Due to its importance in PS imaging, the asymmetric reflection point trajectory has been discussed by various authors (Chung and Corrigan, 1985; Tessmer and Behle, 1988; Yilmaz, 2001; Grechka and Tsvankin, 2002).

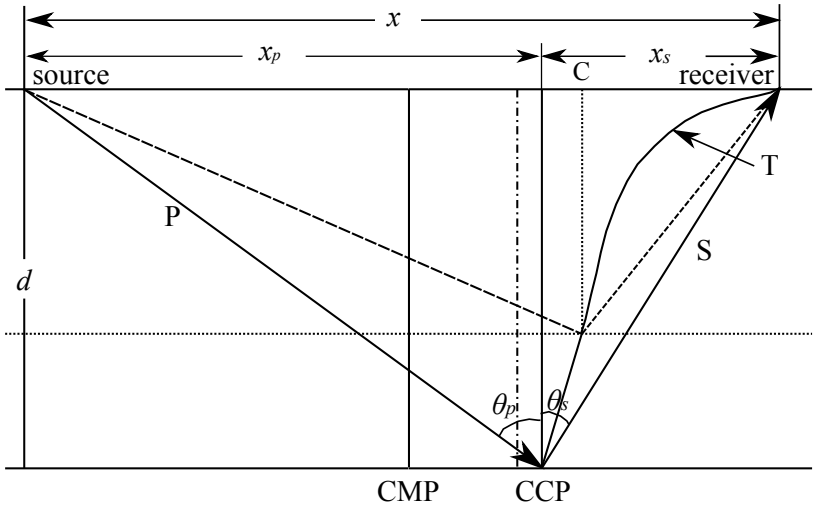

Figure 2.10: Conversion point trajectory (T) at constant V_p/V_s. chapter2/data2 ccp

As can be seen in Figure 2.10, d is the depth of a reflector, x is the offset, θ_p is the incident angle of the P-wave, θ_s is the reflection angle of the S-wave, γ equals V_p/V_s.

$$x_p = d \cdot \tan\theta_p \ , \quad x_s = d \cdot \tan\theta_s \ . \tag{2.10}$$

Assuming $\tan\theta \approx \sin\theta$, we have $V_p/V_s = \sin\theta_p/\sin\theta_s \approx \tan\theta_p/\tan\theta_s = x_p/x_s$, thus

$$\begin{aligned} x_p &= x\cdot(V_p/V_s)/(1+V_p/V_s) \\ &= x\cdot\gamma/(1+\gamma) \\ x_s &= x/(1+V_p/V_s) \\ &= x/(1+\gamma) \end{aligned} \tag{2.11}$$

Converted Wave Traveltime and Normal Moveout

A converted wave propagates as a one-way P-wave plus a one-way S-wave. Hence, for arbitrary depth z_0, as in Figure 2.10 ,

$$t = t_p + t_s = \frac{1}{V_p}\sqrt{z_0^2+x_p^2} + \frac{1}{V_s}\sqrt{z_0^2+x_s^2}\,. \tag{2.12}$$

Converted-wave traveltime can be expressed in P-wave travel time. $t_{p0} = 2z_0/V_p$, thus,

$$t = t_p + t_s = \sqrt{\frac{t_{p0}^2}{4}+\frac{x_p^2}{V_p^2}} + \sqrt{\frac{t_{p0}^2V_p^2}{4V_s^2}+\frac{x_s^2}{V_s^2}} = \sqrt{\frac{t_{p0}^2}{4}+\frac{x_p^2}{V_p^2}} + \sqrt{\frac{t_{p0}^2\gamma^2}{4}+\frac{x_s^2}{V_s^2}} \tag{2.13}$$

A converted-wave can also be described in S-wave travel time. $t_{s0} = 2z_0/V_s$, hence,

$$t = t_p + t_s = \sqrt{\frac{t_{s0}^2V_s^2}{4V_p^2}+\frac{x_p^2}{V_p^2}} + \sqrt{\frac{t_{s0}^2}{4}+\frac{x_s^2}{V_s^2}} = \sqrt{\frac{t_{s0}^2}{4\gamma^2}+\frac{x_p^2}{V_p^2}} + \sqrt{\frac{t_{s0}^2}{4}+\frac{x_s^2}{V_s^2}} \tag{2.14}$$

Equation 2.13 indicates that having V_p, V_s, depth z_0, and x_s we can register a converted-wave image with a PP-wave image. It provides a potential solution to multicomponent data correlation and registration.

Multicomponent data processing experience tells us that PS data exhibit strong nonhyperbolic moveout behavior. The best-fit hyperbola (Tessmer and Behle, 1988) $t = t_0^2 + \frac{x^2}{V_{nmo}^2}$ to the traveltime trajectory associated with a PS reflection on a CCP gather does not work well. Hence,

velocity analysis using the nonhyperbolic moveout equation has been suggested (Yilmaz, 2001),

$$t = \sqrt{\frac{t_{ps0}^2 V_p^2 V_s^2}{V_p^2 (V_p + V_s)^2} + \frac{x_p^2}{V_p^2}} + \sqrt{\frac{t_{ps0}^2 V_p^2 V_s^2}{V_s^2 (V_p + V_s)^2} + \frac{x_s^2}{V_s^2}} = \sqrt{\frac{t_{ps0}^2}{(1+\gamma)^2} + \frac{x_p^2}{V_p^2}} + \sqrt{\frac{t_{ps0}^2 \gamma^2}{(1+\gamma)^2} + \frac{x_s^2}{V_s^2}}\ , \quad (2.15)$$

where $t_{ps_0} = z_0/V_p + z_0/V_s$, $z_0 = t_{ps0} V_p V_s/(V_p + V_s)$.

Grechka and Tsvankin (2002) suggested abandoning the whole idea of PS-wave moveout, because of problems such as the move-out asymmetry with respect to zero offset in PS-wave velocity analysis and smearing of PS reflections in the presence of lateral heterogeneity. In addition, a polarity reversal near the zero-amplitude trace causes problems for moveout-analysis methods based on coherency measures of the reflected signal. Hence, a reconstructed SS-wave moveout was proposed. An important assumption in their method is the input PP and PS-waves are reflected from the same interface, and correlation of interpreted PP and PS reflections often require borehole data (Tsvankin and Grechka, 2011). An automatic approach to multicomponent seismic image registration (Fomel and Backus, 2003; Fomel et al., 2005) provides a solution for correlating interpreted PP and PS reflections without using log data. In fact, this multistep registration method can also be related to PS-wave moveout analysis.

Chapter 3

Spectral Recomposition and Seismic Attributes Study

Background*

Spectral recomposition splits the seismic spectrum into Ricker components and provides a tool for imaging and mapping temporal bed thicknesses and geologic discontinuities. I propose a separable nonlinear least-squares estimation in spectral recomposition. Employing the Gauss-Newton method, a separable nonlinear least-squares approach estimates fundamental signal parameters: peak frequencies and amplitudes.

Frequency domain seismic data attributes are useful in hydrocarbon reservoir characterizations (Castagna et al., 2003; Li et al., 2011). If a seismic response can be captured at each frequency subset, a reservoir interval of interest can then be analyzed in greater detail. Spectral decomposition is a technique developed at Amoco in the 1990s (Partyka et al., 1999). Various time-frequency analysis methods have been employed for frequency decomposition. Dilay and Eastwood (1995) applied short-time Fourier transform, which suffers from a time-frequency resolution limit (Chakraborty and Okaya, 1995). Liu (2006) and Chen et al. (2008) applied spectral decomposition in the time domain by decomposing the seismogram into constituent wavelets, and then summing the Fourier spectra of individual wavelets. This approach experiences difficulties when the frequency range is large, and it relies on the accuracy of wavelet decomposition, whose residuals commonly introduce bias into "frequency gathers." Liu et al. (2011) implemented spectral decomposition by time-frequency

*Parts of this chapter appeared in Cai et al. (2012).

analysis using local attributes.

Tomasso et al. (2010) defined *frequency recomposition* in seismic forward modeling as estimation of Ricker components of the seismic spectrum by manual picking of component frequencies and amplitudes, which is not accurate and depends on personal skill and experience. I propose spectral recomposition using separable nonlinear least-squares estimation (Golub and Pereyra, 1973), which simultaneously and automatically fits both linear and nonlinear parts of the Ricker wavelet spectrum. This approach provides an accurate and direct estimation of amplitudes and peak frequencies of various Ricker wavelets. A problem is separable if the model can be represented as a linear combination of functions that have a nonlinear parametric dependence. The procedure fits frequencies and amplitudes with large variations, and provides a computing confidence, as well as prediction and calibration intervals. The Gauss-Newton algorithm, a method of minimizing the residual sum of squares, is effective both when residuals are small and when measurement errors are additive and the data set is large (Osborne, 2007). An analogous method was used previously by Browaeys and Fomel (2009) for fitting *von Kármán* distributions, and by Liu et al. (2011) for fitting a single Ricker wavelet.

In this thesis, I represent a seismic spectrum as a sum of different Ricker components. I then use the Gauss-Newton method to fit a seismic spectrum with a combination of several Ricker wavelet spectra so as to estimate the peak frequency and amplitude of each component. Spectral recomposition improves seismic image and helps seismic attribute study on a field data example from the Gulf of Mexico.

Theory

A seismic spectrum can be represented as a composition of a number of different Ricker components (Castagna et al., 2003; Liu, 2006):

$$d(f) \approx \sum_{i=1}^{n} a_i \psi_i(m_i, f) \ , \tag{3.1}$$

where $d(f)$ is the spectrum of a seismic trace, and a_i and m_i are the amplitude and peak frequency of the i-th Ricker spectrum component, given as

$$R(f) = a\, \psi(m, f) = a\, \frac{f^2}{m^2}\, exp(-\frac{f^2}{m^2}) \ . \tag{3.2}$$

The model is a linear combination of Ricker wavelet spectra, which has nonlinear functions and depends on multiple parameters. To estimate the Ricker wavelet spectra, we need both $\mathbf{a} = \{a_1, a_2, ..., a_n\}$ and $\mathbf{m} = \{m_1, m_2, ..., m_n\}$ coefficients. Let

$$r_j(\mathbf{a}, \mathbf{m}) = d(f_j) - \sum_{i=1}^{n} a_i(\mathbf{m}) \psi_i(m_i, f_j) \ . \tag{3.3}$$

The optimal least-squares estimation requires

$$\min_{\mathbf{a},\mathbf{m}} \|\mathbf{r}(\mathbf{a}, \mathbf{m})\|_2^2 \ . \tag{3.4}$$

The goal of separable nonlinear least-squares estimation (Björck, 1996) is to find a global minimizer of the sum of squares of nonlinear functions. The separability aspect comes from solving linear and non-linear parts separately (Scolnik, 1972). The algorithm used in this paper is known as the variable projection algorithm (Golub and Pereyra, 1973), which is based on separable nonlinear least squares. This approach provides solutions for $\mathbf{a}$ and $\mathbf{m}$.

Numerical Method

In a general case, we want

$$\min \left\| d(f) - \begin{bmatrix} \psi_1(m_1, f) & \psi_2(m_2, f) & ... & \psi_n(m_n, f) \end{bmatrix} \begin{bmatrix} a_1 \\ a_2 \\ ... \\ a_n \end{bmatrix} \right\|_2^2 . \tag{3.5}$$

If we know the nonlinear parameters of $\mathbf{m}$, then the linear parameters of $\mathbf{a}$ can be obtained by solving the linear least-squares problem ,

$$\mathbf{a} = \boldsymbol{\psi}(\mathbf{m})^{\dagger}\mathbf{d} , \tag{3.6}$$

where $\boldsymbol{\psi}(\mathbf{m})$ is the matrix composed of $\psi_i(m_i, f_j)$, and $\boldsymbol{\psi}(\mathbf{m})^{\dagger}$ is the Moore-Penrose generalized inverse of the $\boldsymbol{\psi}(\mathbf{m})$ matrix. Let

$$\boldsymbol{\gamma} = a_1\boldsymbol{\psi_1} + a_2\boldsymbol{\psi_2} + ... + a_n\boldsymbol{\psi_n} - \mathbf{d} \approx 0 ,$$

and

$$\begin{aligned} Q(a_1, a_2, ..., a_n) &= \boldsymbol{\gamma} \cdot \boldsymbol{\gamma} \\ &= (a_1\boldsymbol{\psi_1} + a_2\boldsymbol{\psi_2} + ... + a_n\boldsymbol{\psi_n} - \mathbf{d}) \cdot (a_1\boldsymbol{\psi_1} + a_2\boldsymbol{\psi_2} + ... + a_n\boldsymbol{\psi_n} - \mathbf{d}) . \end{aligned}$$

The gradient of $Q(a_1, a_2, ..., a_n)$ is defined by n components:

$$\begin{aligned} \frac{\partial Q}{\partial a_1} &= \boldsymbol{\psi_1}(a_1\boldsymbol{\psi_1} + a_2\boldsymbol{\psi_2} + ... + a_n\boldsymbol{\psi_n} - \mathbf{d}) + (a_1\boldsymbol{\psi_1} + a_2\boldsymbol{\psi_2} + ... + a_n\boldsymbol{\psi_n} - \mathbf{d})\boldsymbol{\psi_1} \\ \frac{\partial Q}{\partial a_2} &= \boldsymbol{\psi_2}(a_1\boldsymbol{\psi_1} + a_2\boldsymbol{\psi_2} + ... + a_n\boldsymbol{\psi_n} - \mathbf{d}) + (a_1\boldsymbol{\psi_1} + a_2\boldsymbol{\psi_2} + ... + a_n\boldsymbol{\psi_n} - \mathbf{d})\boldsymbol{\psi_2} \\ &..... \\ \frac{\partial Q}{\partial a_n} &= \boldsymbol{\psi_n}(a_1\boldsymbol{\psi_1} + a_2\boldsymbol{\psi_2} + ... + a_n\boldsymbol{\psi_n} - \mathbf{d}) + (a_1\boldsymbol{\psi_1} + a_2\boldsymbol{\psi_2} + ... + a_n\boldsymbol{\psi_n} - \mathbf{d})\boldsymbol{\psi_n} \end{aligned}$$

Setting these derivatives to zero, we are able to sovle for $\mathbf{a}$

$$\begin{bmatrix} a_1 \\ a_2 \\ ... \\ a_n \end{bmatrix} = \begin{bmatrix} \int_f \psi_1^2 & \int_f \psi_1\psi_2 & ... & \int_f \psi_1\psi_n \\ \int_f \psi_2\psi_1 & \int_f \psi_2^2 & ... & \int_f \psi_2\psi_n \\ ... & ... & ... & ... \\ \int_f \psi_n\psi_1 & \int_f \psi_n\psi_2 & ... & \int_f \psi_n^2 \end{bmatrix}^{-1} \begin{bmatrix} \int_f d(f)\psi_1 \\ \int_f d(f)\psi_2 \\ ... \\ \int_f d(f)\psi_n \end{bmatrix} . \tag{3.7}$$

Replacing $\mathbf{a}$ in the original function, the minimization problem takes the form

$$\min_{\mathbf{m}} \left\| (\boldsymbol{I} - \boldsymbol{\psi}(\mathbf{m})\boldsymbol{\psi}(\mathbf{m})^{\dagger})\mathbf{d} \right\|_2^2 , \tag{3.8}$$

where the linear parameters have been eliminated (Golub and Pereyra, 1973). I use the Gauss-Newton method (Björck, 1996) to compute the solution by linearization

$$\begin{aligned} d(f) &\approx R(\mathbf{m}, f) + \frac{\partial R}{\partial \mathbf{m}}\Delta\mathbf{m} \\ &\approx \mathbf{a}\,\psi(\mathbf{m}, f) + [\mathbf{a}'(\mathbf{m})\,\psi(\mathbf{m}, f) + \mathbf{a}\,\psi'(\mathbf{m}, f)]\Delta\mathbf{m}. \end{aligned}$$

To solve for $\mathbf{a}'$, we have

$$\begin{aligned} \boldsymbol{\Psi}^T\mathbf{d} &= (\boldsymbol{\Psi}^T\boldsymbol{\Psi} + \mathbf{I}\epsilon^2)\mathbf{a} \\ (\boldsymbol{\Psi} + \boldsymbol{\Delta\Psi})^T\mathbf{d} &= ((\boldsymbol{\Psi} + \boldsymbol{\Delta\Psi})^T(\boldsymbol{\Psi} + \boldsymbol{\Delta\Psi}) + \mathbf{I}\epsilon^2)(\mathbf{a} + \boldsymbol{\Delta}\mathbf{a}) \\ \boldsymbol{\Delta\Psi}^T\mathbf{d} &= (\boldsymbol{\Delta\Psi}^T\boldsymbol{\Psi} + \boldsymbol{\Psi}^T\boldsymbol{\Delta\Psi})\mathbf{a} + (\boldsymbol{\Psi}^T\boldsymbol{\Psi} + \mathbf{I}\epsilon^2)\boldsymbol{\Delta}\mathbf{a} , \end{aligned}$$

hence,

$$\mathbf{a}' = (\boldsymbol{\Psi}^T\boldsymbol{\Psi} + \mathbf{I}\epsilon^2)^{-1}[(\boldsymbol{\Psi}')^T\mathbf{d} - [(\boldsymbol{\Psi}')^T\boldsymbol{\Psi} + \boldsymbol{\Psi}^T\boldsymbol{\Psi}']\mathbf{a}] . \tag{3.9}$$

Since

$$\gamma(f) \approx \begin{bmatrix} (\psi_1 a_1'(m_1, ..., m_n) + \psi_1' a_1) & ... & (\psi_n a_n'(m_1, ..., m_n) + \psi_n' a_n) \end{bmatrix} \begin{bmatrix} \Delta m_1 \\ ... \\ \Delta m_n \end{bmatrix} , \tag{3.10}$$

we will be able to solve for Δm.

That is, starting with initial values of $\mathbf{m}$, we solve for $\mathbf{a}$ and $\mathbf{a}'$, using equation 3.6. Then we can solve for $\Delta\mathbf{m}$. After a number of iterations, summation of $\Delta\mathbf{m}$ converges. In most cases,

approximately 20 iterations provide an acceptable convergence and generally, fitting more component frequencies would minimize the residual. Geological factors can help a user decide how many components to fit in the model. In addition, providing good initial values helps the algorithm avoid being trapped in a local minimum.

Application

To test the method, I generated a wavelet composed of three Ricker wavelets with peak frequencies of 10, 20 and 50 Hz (Figure 3.1). Applying a separable nonlinear least-squares estimation, estimated peak frequencies are 9.999, 19.999, and 49.995 Hz. The residual sum of squares equals about 10^{-7} after about 50 iterations. As can be seen in Figure 3.1, the computed spectrum and its estimation are consistent with one another.

The concept behind spectral recomposition is that the seismic reflection has a characteristic expression in the frequency domain that is indicative of its significant components. Hence, spectral recomposition can be used in seismic interpretation, especially horizontal or stratal slice imaging. I used data from Starfak and Tiger Shoal fields of offshore Louisiana, a 135-mile^2 3-D survey area. The study area lies along the western periphery of the ancestral Mississippi River depocenter (McGookey, 1975), most recently designated the central Mississippi sediment-dispersal axis by Galloway et al. (2000) and Zeng and Hentz (2004).

Geological factors help decide the number of component frequencies needed to fit the model. For example, the real data spectrum has been estimated using three component frequencies in Figure 3.3. Having estimated the parameters, i.e. the peak frequencies and amplitudes, I reconstructed the spectrum for each Ricker wavelet.

Spectral recomposition indicates the significant component frequencies. Setting the fre-

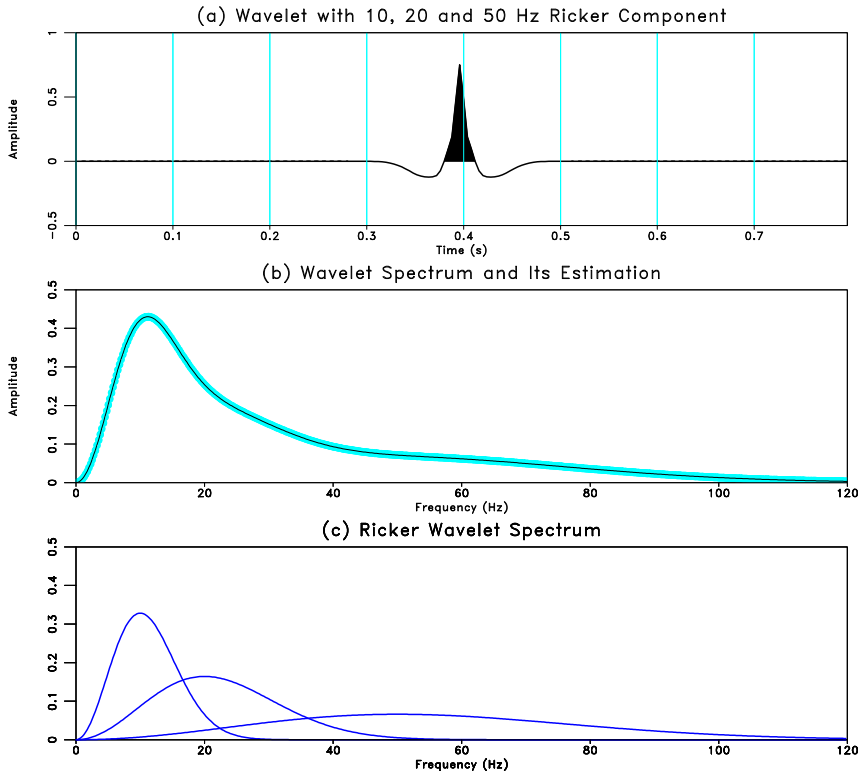

Figure 3.1: (a) A wavelet and (b) its spectrum composed of three Ricker components, with peak frequencies 10, 20 and 50 Hz. (c) Estimated wavelet spectrum components. Estimated peak frequencies of these Ricker components are 9.999, 19.999 and 49.995 Hz. chapter3/ricker rk

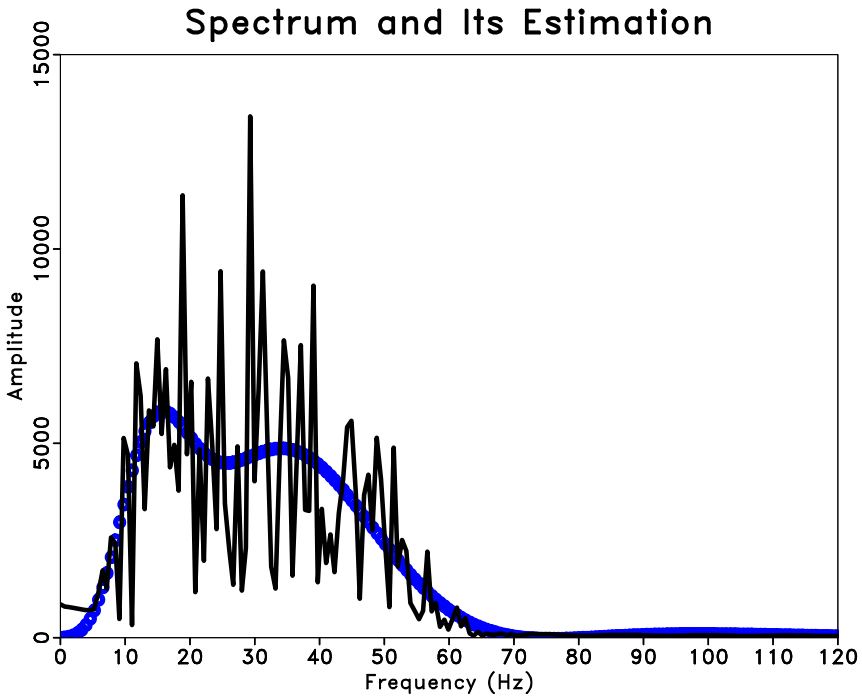

Figure 3.2: Seismic spectrum and its estimation. chapter3/gulf check

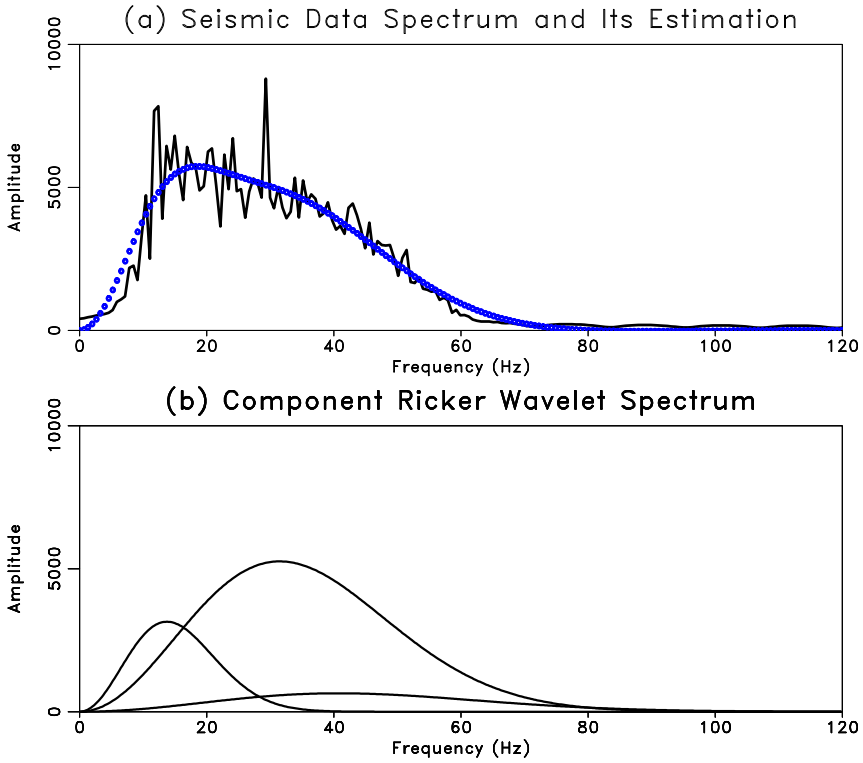

Figure 3.3: (a) Spectrum of seismic data from Tiger Shoal. (b) Estimated seimic spectrum components. chapter3/gulf recomp

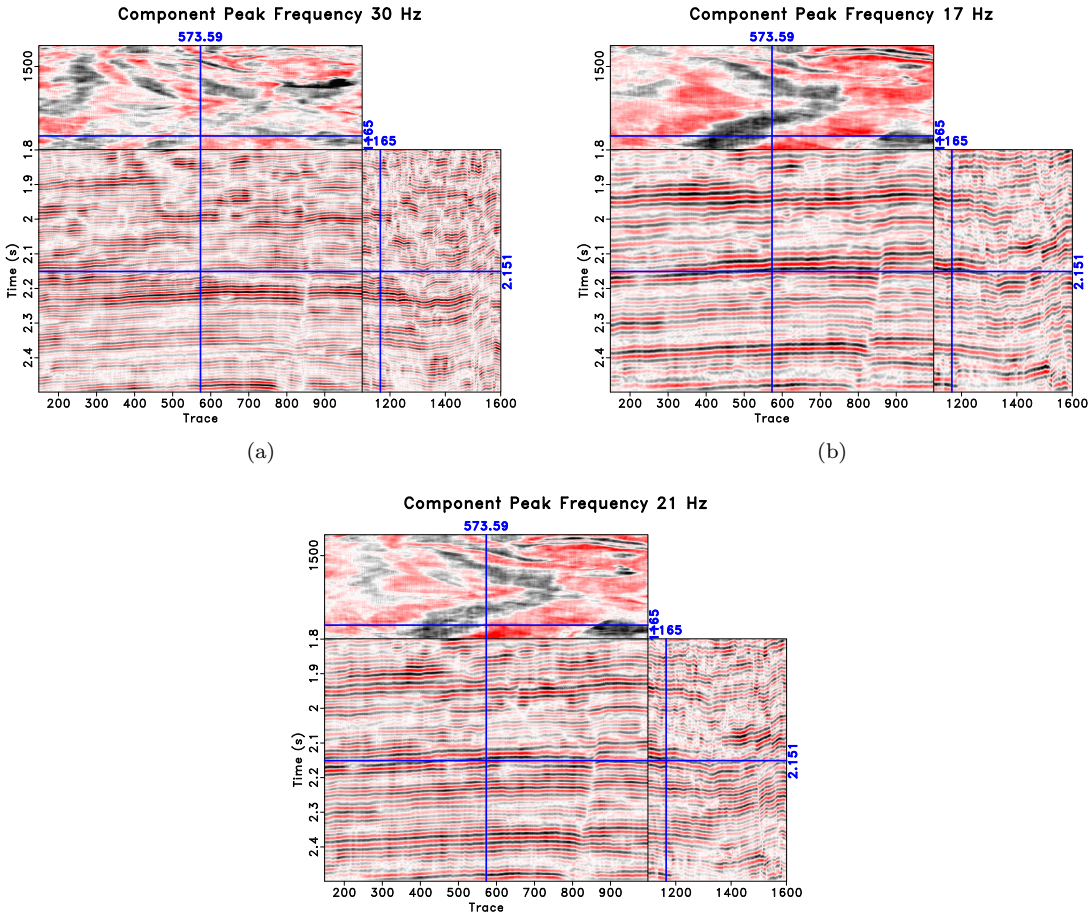

Figure 3.4: (a) Seismic volume from Tiger Shoal area displayed with manually picked frequency bandpass filter. (b) and (c) The same volume displayed, using two components of spectral recomposition. A fault system clearly shows up in both (b) and (c). chapter3/gulf sgr330,sgr317,sgr321

quencies and their bandwidths yields Figure 3.4(b) and 3.4(c). I have previously picked a different frequency to display the same seismic section as appears in Figure 3.4(a) on the basis of experience. Comparing these two figures, I found Figure 3.4(b) and 3.4(c) to provide better images. Reflections and seismic events are displayed better, for example in Figure 3.4(b) and 3.4(c). A fault system also clearly shows up in both Figure 3.4(b) and 3.4(c), but is less obvious in Figure 3.4(a).

Spectral recomposition helps us improve the image of horizontal slices as well. Zeng and Hentz (2004) constructed and interpreted stratal slices as in Figure 3.5(a) by using special tools to restore and refine multiple seismic slices in the wire-line-log context in both the traveltime domain and the relative geologic-time domain. Their approach includes conditioning seismic data to log lithology by 90^o phasing to achieve better well log integration, imaging, and interpretation of the sequential, planoform geomorphology of the depositional systems (Zeng and Backus, 2005a,b). Our goal is to use spectral recomposition to help improve seismic imaging, and compare our results with those of Zeng and Hentz (2004). Both Figure 3.5(b) and Figure 3.5(c) plot the region inside the dashed line in Figure 3.5(a), which displays results from Zeng and Hentz (2004). Without applying spectral recomposition, I can barely see any geologic features or depositional systems in Figure 3.5(b). Using spectral recomposition, I then set the frequency bandpass filter. The incised valley fill (IVF), highstand delta, and point bar and distributary channels can easily be recognized in Figure 3.5(c). Compared with Figure 3.5(b), Figure 3.5(c) provides solid geological information. I used color blending plotting (Chopra and Marfurt, 2007) to plot three components in Figure 3.6. Compared with Figure 3.5(c), more details can be seen in Figure 3.6. Hence, when spectral recomposition is used, geological features can be identified in stratal slices.

Spectral recomposition indicates how various frequency components attenuate in the subsurface. To prepare for multicomponent seismic attributes study in Chapter 3, I analyzed and modeled

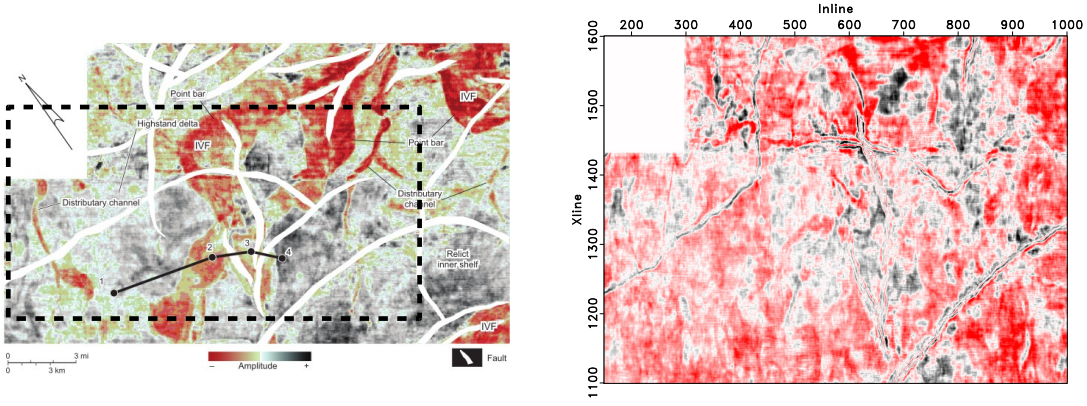

(a) (b)

(c)

Figure 3.5: (a) A stratal slice picked by Zeng and Hentz (2004). (b) A stratal slice picked without using spectral recomposition. We barely recognize any deposition system in the stratal slice. (c) A stratal slice picked by using spectral recomposition. We find various deposition systems, such as incised valley fill, distributary channels and point bars in the slice. chapter3/slice sgr,sgr3slice,sgr316

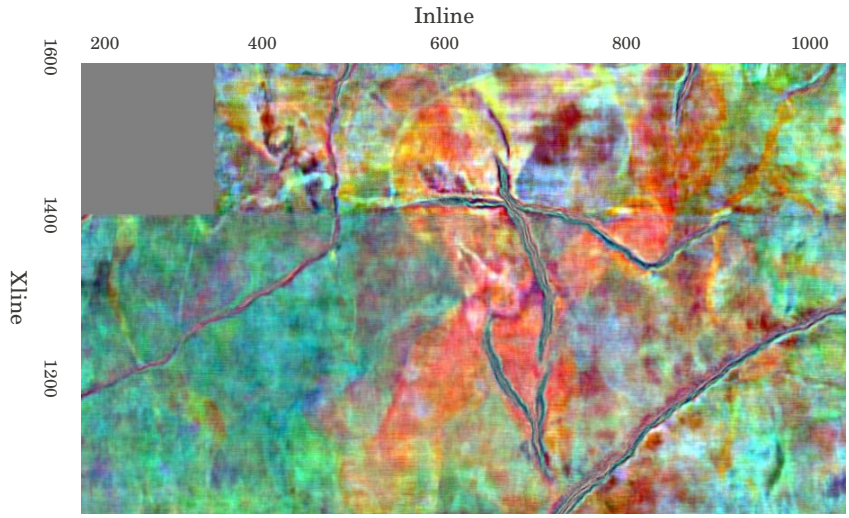

Figure 3.6: Three components of Tiger Shoal stratal slice have been picked and plotted by using color blending, which provides more detailed information. chapter3/slice sgr3

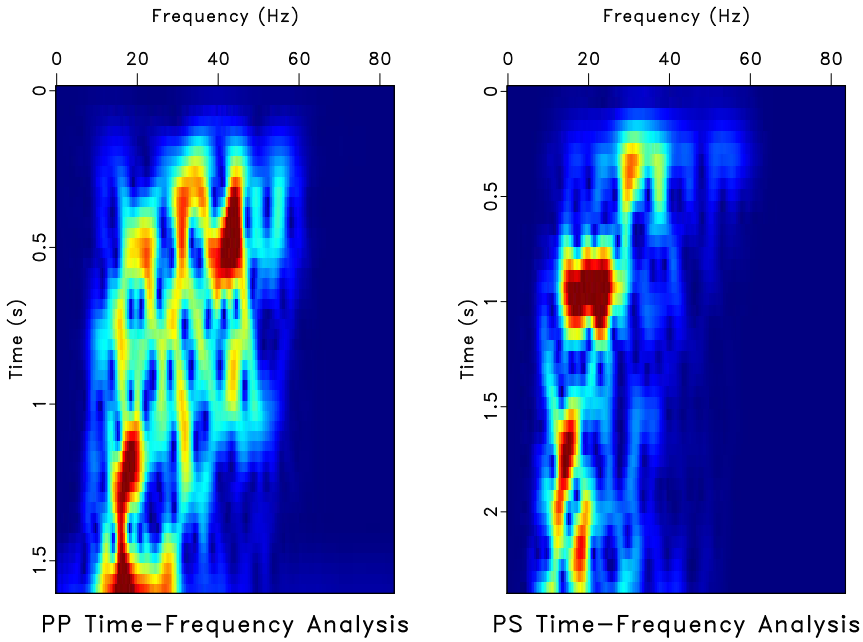

Figure 3.7: Time-frequency analysis of PP-wave and PS-wave traces. chapter3/tf ltft2

frequency components of multicomponent seismic data by using spectral recomposition. With the help of local time-frequency analysis (Liu et al., 2011), I recomposed the spectra of a seismic trace at different time depths. Around 0.5 second, the component of the PP trace has a peak frequency as high as 45 Hz. As can be seen, the high-frequency PP component attenuates gradually to 25 Hz at 1.6 seconds. For the component of PS trace, it has a peak frequency as high as 30 Hz at about 1 second, and then gradually attenuates to 20 Hz at about 2 seconds. When spectra of a seismic trace are recomposed at different time depths, the spectral recomposition provides information related to any specific layer the user might be interested in and helps toward a deeper understanding of seismic attenuation in the subsurface.

Spectral recomposition can also be used to estimate thin bed thickness and to search for

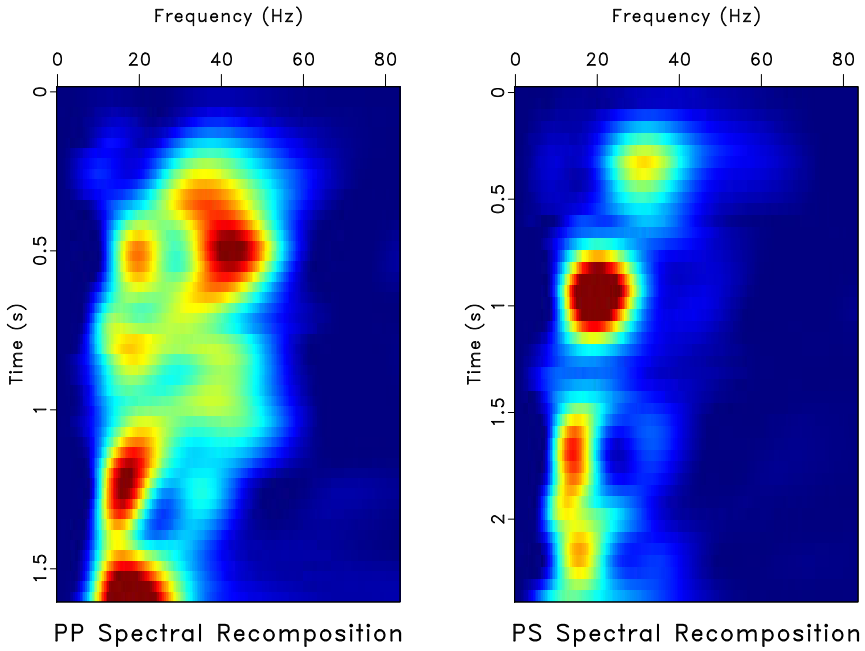

Figure 3.8: Using spectral recomposition, I analyze the spectra of PP-wave and PS-wave traces. chapter3/tf specrecom2

tuning frequency. The technique provides a robust and phase-independent approach to seismic thickness estimation. Compared with conventional methods involving adjacent peaks and troughs, spectral recomposition requires simply peak frequency and amplitude estimation. With separable non-linear least squares estimation, we can easily estimate dominant frequencies, which may lead to improved tuning thickness estimation.

Conclusions

Spectral recomposition using separable nonlinear least squares represents the seismic spectrum as a sum of Ricker components with estimated peak frequencies and amplitudes. With the reconstructed seismic spectrum from component frequencies, spectral recomposition can be used in seismic data interpretation.

Applying spectral recomposition, I have been able to improve seismic imaging from the Tiger Shoal area. This procedure revealed various depositional systems in the stratal slice, which can barely be detected otherwise. The method may also be used in forward modeling as well to provide detailed information about different layers in the subsurface. To apply separable nonlinear least-squares estimation for spectral recomposition, interpreters and processors may need to use principal component analysis to decide how many components to fit into the model. Appendix contains the C code and Madagascar' script I used for spectral recomposition. Madagascar (http://www.ahay.org) is an open-source software package for multidimensional data analysis and reproducible computational experiments.

Chapter 4

Multicomponent Seismic Image Registration

Image Registration

Image registration has been widely used in different areas, such as medical imaging and geographic information systems (GIS). Image registration is the process of overlaying two or more images of the same scene taken at different times, from different viewpoints, and/or by different sensors (Zitová and Flusser, 2003). The image registration problem can be phrased in only a few words: given a reference and a template image, find a suitable transformation such that the transformed template becomes similar to the reference (Modersitzki, 2004). In other words, the task of image registration is to find an optimal geometric transformation to align the reference image and the sensed image.

Application of image registration can be divided into groups according to the manner of the image acquisition (Zitová and Flusser, 2003): different view points, different times, different sensors, and different scenes to register. The majority of the registration methods consist of the following four steps (Zitová and Flusser, 2003): feature detection, feature matching, transform model estimation, and image resampling and transformation. We will see these steps specified and applied in the multistep approach to multicomponent image registration.

Geometric transformation alone can barely achieve good registration result, because seismic attributes play an important role in multicomponent seismic image registration. Using seismic spectrum recomposition, I studied multicomponent seismic attributes in this thesis. I then applied

an automatic approach (Fomel et al., 2005), which registers images of multicomponent seismic data with various tools including local frequency and local similarity analysis. Registering the multicomponent seismic images step by step, I standardize the work flow of this automatic and multistep approach. The related seismic characters and attributes are discussed and studied in this thesis.

PP and PS Image Registration

Rapid advancements in both land and marine multicomponent data acquisition and processing leads to numerous applications of converted-wave data in exploration and production. Multicomponent seismic data have been increasingly used in structural imaging, lithology estimation, anisotropy analysis, subsurface fluid description, and reservoir monitoring (Stewart et al., 2003; Hardage et al., 2011). However, from the interpreter's point of view, multicomponent data present numerous difficulties and uncertainties (Cary, 2001). Most interpretation packages used in the industry do not work well for multicomponent data imaging and interpretation. The registration of PP and PS data remains a topic of concern among interpreters, as well as a focus of technology development.

More than 25 years ago, when researchers talked about the future of shear wave exploration, a couple of questions were significantly important to them, one of which was correlation of S-wave and P-wave reflection (Danbom and Domenico, 1987). Correlating S-wave reflection with P-wave reflection is one of the very first steps and one of the crucial steps in multicomponent data interpretation. In a given stratigraphic interval of the geologic section, registration correlates the P- and S-wave profiles to determine t_s/t_p ratio, which is equivalent to V_p/V_s for a vertical propagation path. The registration process (event matching between the PP, PS and SS) is largely driven by the availability of dipole sonic logs. However, these dipole sonics are not as common as standard sonic logs and tend to be more affected by washouts and other problems with the borehole (Hardage

et al., 2011). Therefore, we need new techniques for accurate correlation and registration.

Theoretically, PS-wave data should add significant information to the conventional PP-wave interpretation. In practice, it is often difficult to use PS-wave information directly in an integrated interpretation because of difficulties in the registration of events between the PP-wave and PS-wave datasets. Inverting both PP-wave and PS-wave seismic volumes can facilitate the integrated interpretation of datasets by converting them to P and S impedance estimates which are more directly related to rock properties (Garotta et al., 2002). However, inverting the datasets independently can lead to incorrect estimates of V_p/V_s ratio because the inversions optimize each property in isolation (Hirsche et al., 2005). Jointly inverting PP-wave and PS-wave seismic volumes accounts for the physical relationship that exists between P-impedance, S-impedance, and density and provides a significant improvement over separate inversions of the two datasets, particularly for V_p/V_s ratio estimates. Joint inversion of PP and PS data can be helped by registration of PS data to PP time.

Two important assumptions are related to multicomponent seismic image registration (Hardage et al., 2011):

1. Across some stratigraphic intervals, one mode of an elastic wavefield might show different seismic sequences and facies than its companion modes do.

2. We expect a data window of converted wave image to match the data window of P-wave image, which requires the same reflecting horizon be identified on both data sets.

In other words, if all different modes show exactly the same seismic sequence and facies, there is no need for us to require multicomponent data. S-wave seismic sequences and facies are just as important in geologic interpretation as P-wave seismic sequences and facies. However, since all

different modes are acquired from the same region, we would expect similarity and correlation. The interpreter needs to decide which S-wave reflection event occurs at the same stratigraphic boundary where a P-wave reflection event has been interpreted.

Different methods have been proposed and developed for P and S wave correlation and depth registration. Tatham et al. (1991) discussed using faulting, overall structural character and stratigraphic sequence boundaries in P and S wave correlation. If available, borehole logging and vertical seismic profile (VSP) provide more reliable information (DeAngelo et al., 2003). Hardage et al. (2011) describe the recent development in depth registration methods,

- Depth registration using VSP data
- Depth registration using V_p and V_s velocities
- Depth registration using thin-bed stratigraphy
- Depth registration using structure
- Depth registration by interpreter judgment
- Numerical registration of P and S data using vertical slices
- Numerical registration of P and S data using horizontal slices

VSP data has the advantage in registration in terms of accuracy, because VSP data describe geological events in both time and depth domains. It is the most definitive data that can be used to establish a rigorous transformation between stratigraphic depth and seismic image time for any wave mode defined by a VSP wavefield Hardage et al. (2011).

V_p and V_s velocities can also be used for depth registration. We adjust the traveltime axes

of surface-recorded P and S data so that P and S events from depth-equivalent interfaces occur at the same image times. A converted wave propagates as a one-way P-wave plus a one-way S-wave. Having P-wave and S-wave velocity, it is easy to determine traveltime of a converted wave. If distance between source and converted point C is x_p, the distance between converted point C and receiver is x_s, and the depth is z_0, the converted-wave traveltime is:

$$t = t_p + t_s = \frac{1}{V_p}\sqrt{z_0^2 + x_p^2} + \frac{1}{V_s}\sqrt{z_0^2 + x_s^2}\,. \tag{4.1}$$

The corresponding PS-wave zero-offset two-way traveltime is $t = z_0/V_p + z_0/V_s$. We may also express PS-wave traveltime in PP-wave travel time.

$$t = t_p + t_s = \sqrt{\frac{t_{p0}^2}{4} + \frac{x_p^2}{V_p^2}} + \sqrt{\frac{t_{p0}^2 V_p^2}{4V_s^2} + \frac{x_s^2}{V_s^2}} = \sqrt{\frac{t_{p0}^2}{4} + \frac{x_p^2}{V_p^2}} + \sqrt{\frac{t_{p0}^2 \gamma^2}{4} + \frac{x_s^2}{V_s^2}}\,, \tag{4.2}$$

where t_{p0} is P-wave vertical two-way traveltime, and γ is the V_p/V_s ratio.

In addition, geologic structure, thin-bed stratigraphy, and interpreter judgment can do depth registration, e.g. if both P and S data image a thin-bed, adjusting P and S images until equivalent thin-bed features appear in both image spaces results in depth-registering P and S image times to reasonable accuracy (DeAngelo et al., 2003).

Several numerical methods have been developed to automate the process of multicomponent image registration, including an algorithm for pairwise alignment of seismic traces (Liner and Clapp, 2004) and a least-squares optimization (Fomel and Backus, 2003; Nickel and Sonneland, 2004). However, unless the images are properly preprocessed to minimize the inevitable differences in amplitude and frequency content, these automatic approaches will fail (Fomel et al., 2005). Fomel and Backus (2003) and Fomel et al. (2005) developed a multistep approach that takes all the differences into consideration while automatically extracting a high-resolution mapping of PS reflection events to the corresponding PP times. Recently developed techniques, such as local similarity measurement

(Fomel, 2007a) are used to help improve image registration.

Initial Registration

Without dipole logs and multicomponent VSP data, PP and PS wave correlation depends on an interpreter's experience. DeAngelo et al. (2003) search characteristic features that should be expected on both PP and PS data sets, and thus provide a correlation basis or "nail" points. Analyzing seismic events, we are able to correlate geological events in a PP wave data volume with events in a PS wave data volume. We then manually pick events in the PP wave data volume and match those events in the PS wave data volume. PS wave traveltime has been preliminarily correlated with PP wave travel time in Figure 4.2. Figure 4.2 also indicates a liner relationship between V_p and V_s.

Assuming reflection events have been correctly positioned laterally in the migrated image, and the difference between PP wave image and PS wave image can only be explained by vertical transformation, we then shall be able to apply a warping function. Warping is originally a signal processing correction (Wolberg, 1990), and is widely used in electronic engineering such as audio signal processing. Setting PP traces as a reference coordinate system, we are able to stretch or squeeze the PS traces accordingly while keeping the signal pattern of PS wave data unchanged. If a PP wave seismic image is denoted as $P(t)$ and a PS wave image is denoted as $C(\tau)$, then the relationship between these two images can be expressed as (Fomel and Backus, 2003)

$$P(t) \approx a(t)C[w(t)] \,, \tag{4.3}$$

where $w(t)$ is the warping function, and $a(t)$ is the amplitude gain function compensating for the differences in reflectivity. That is, we just need to project PS wave traveltime onto PP wave traveltime coordinate system. Thus, the depth-dependent ratio of the P wave and S wave velocities

expressed in the PP wave traveltime coordinate is simply related to the derivative of the warping function (Fomel and Backus, 2003)

$$\gamma(t) = 2w'(t) - 1 \ . \tag{4.4}$$

Reiterating equation 4.4 in terms of interval relationship, we have

$$\gamma(t) = 2\frac{\Delta\tau}{\Delta t} - 1 \ , \tag{4.5}$$

where Δt is time thickness of a layer (Stewart et al., 2002).

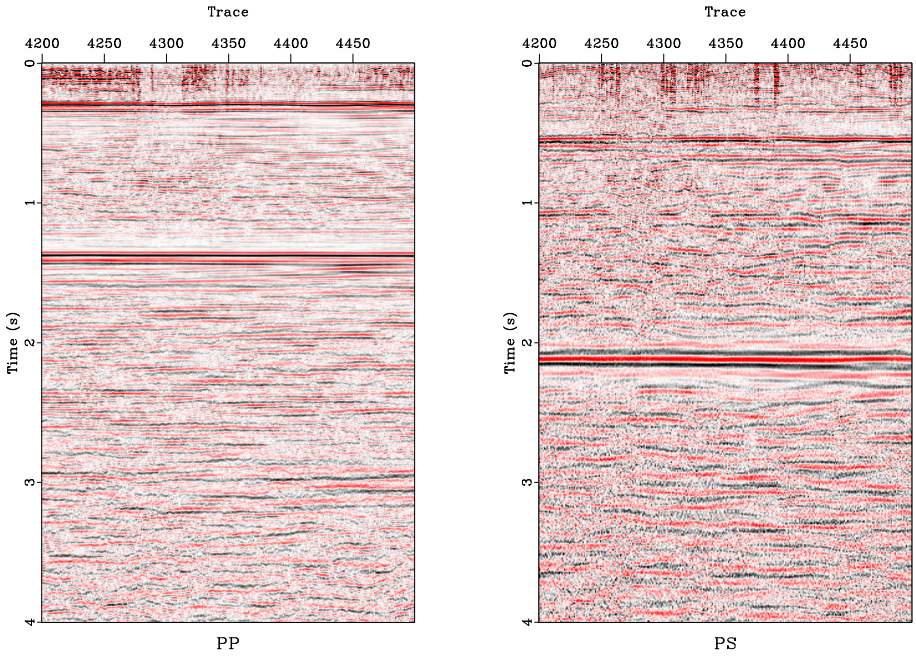

Figure 4.1: PP-wave image (left) and PS-wave image (right) chapter4/registration comp

In this thesis, I sliced the data to show how I can register the seismic events at about 0.6 second and 2.2 seconds in the PS-section with the corresponding event at about 0.25 second and 1.4 seconds in the PP-section. I picked a PP wave trace and a PS wave trace from both session, and applied a 1-D warping function to the PS wave trace. As we can see in Figure 4.3, the PS trace has

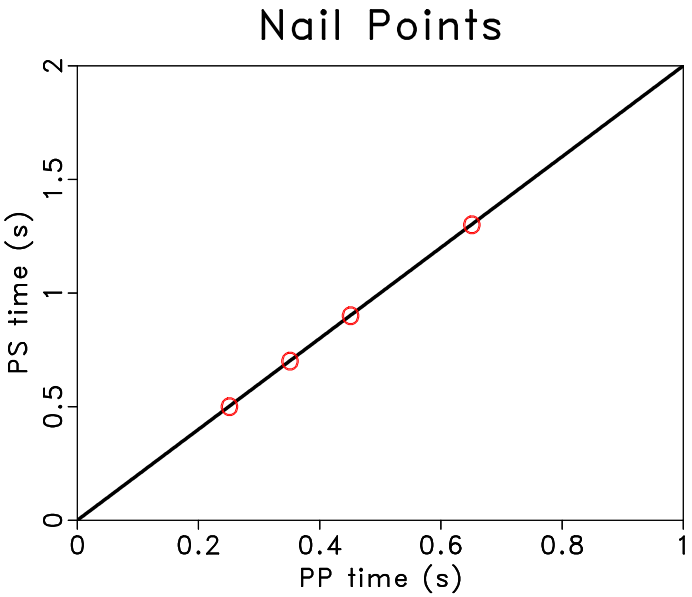

Figure 4.2: In initial registration, we adjust PP and PS images until equivalent features show up on both images, which results in depth-registering PP and PS image times to certain accuracy. This process provides us a correlation basis or nail points. chapter4/registration anails

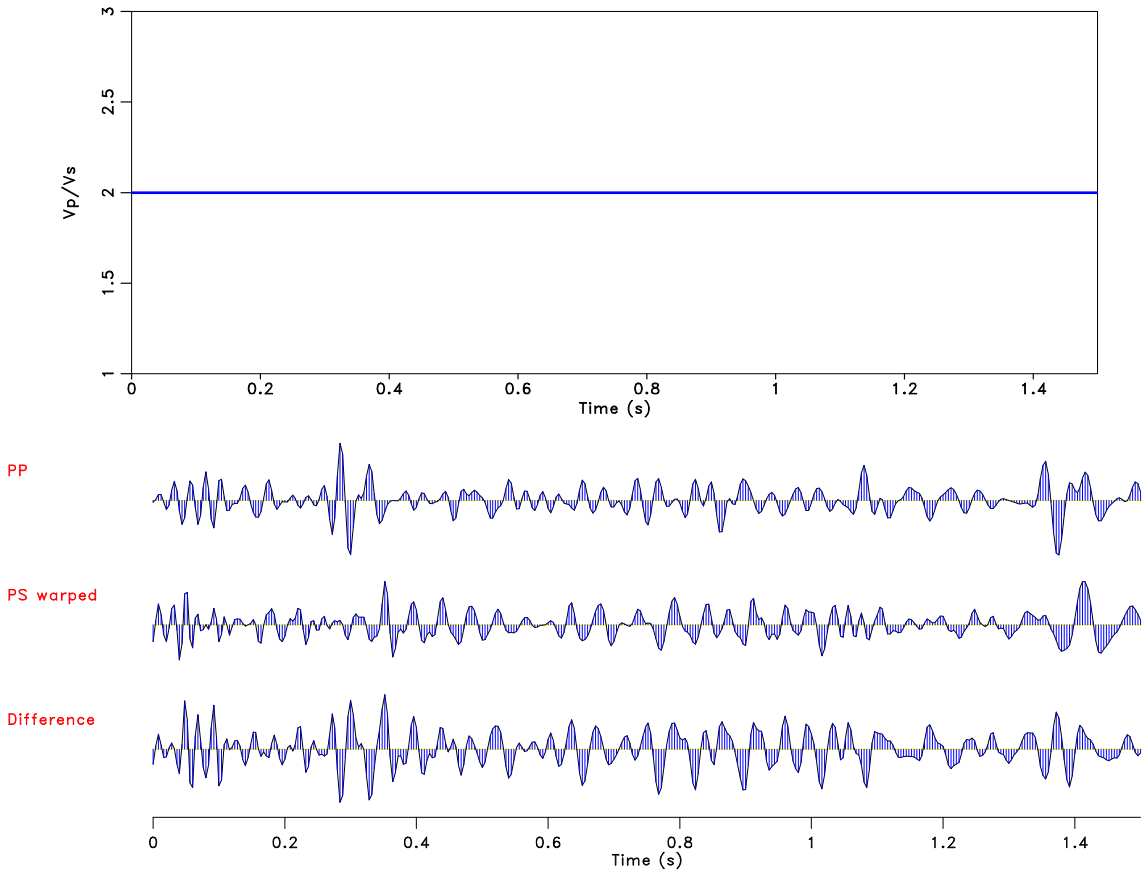

Figure 4.3: The correlation basis indicates a linear relationship between V_p and V_s, hence the plotted V_p/V_s ratio is constant. I picked a PP trace and the corresponding PS trace from seismic section. After initial warping, the PS trace has been squeezed. The warped PS trace partially matches the PP trace. However, the difference between these two traces is still quite large. chapter4/registration apat-psw-0

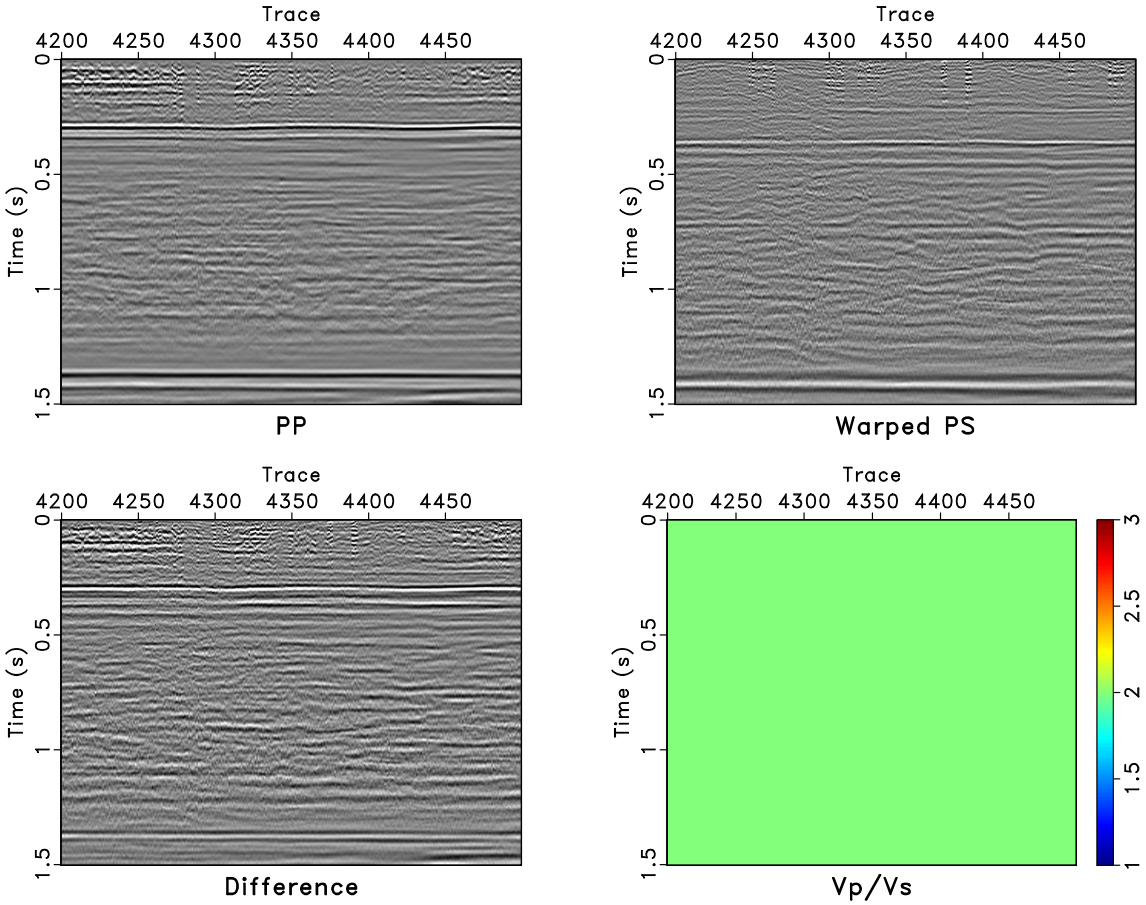

Figure 4.4: Initial registration applies warping function on PS image. The V_p/V_s ratio is constant as indicated by correlation basis. Comparing the warped PS image with the PP image, we find events in the warped PS image match their counterparts in time axes. The difference between two images is larger than desired. chapter4/registration apa-psw-0

been squeezed. We see similarities between the warped PS wave trace and the PP trace, but the difference between those two traces is large. We then applied a warping function on the PS wave image. Figure 4.4 shows the initial registration result. Again, we see a constant V_p/V_s ratio, which is indicated by correlation basis or nail points. Some events in the warped PS image match events in PP image. However, the difference between these two is quite large. Further efforts are needed to improve the warped PS image.

Spectral Balancing

The spectra of PP wave and PS wave are usually different, because the component frequencies are attenuated differently during wave propagation. As discussed in previous chapters, a PP wave typically has more high component frequencies. Such differences between PP wave and PS wave images are a major problem, which prevents an automatic registration process (Fomel and Backus, 2003). Thus, it is required to measure the amplitude and spectral differences and compensate for them before we apply an automatic registration algorithm.

A collection of seismograms is spectrally balanced if they have been filtered so that they all have approximately the same spectrum (Claerbout, 1975). Spectral balancing is often helpful when timing relationships among traces are important. Spectral balancing can be done by deconvolution followed by bandpass filtering. In our example, smooth estimation of instantaneous frequency has been applied to estimate local frequency, which is an important local seismic attribute (Fomel, 2007a). We applied non-stationary spectral balancing to compensate the frequency and amplitude.

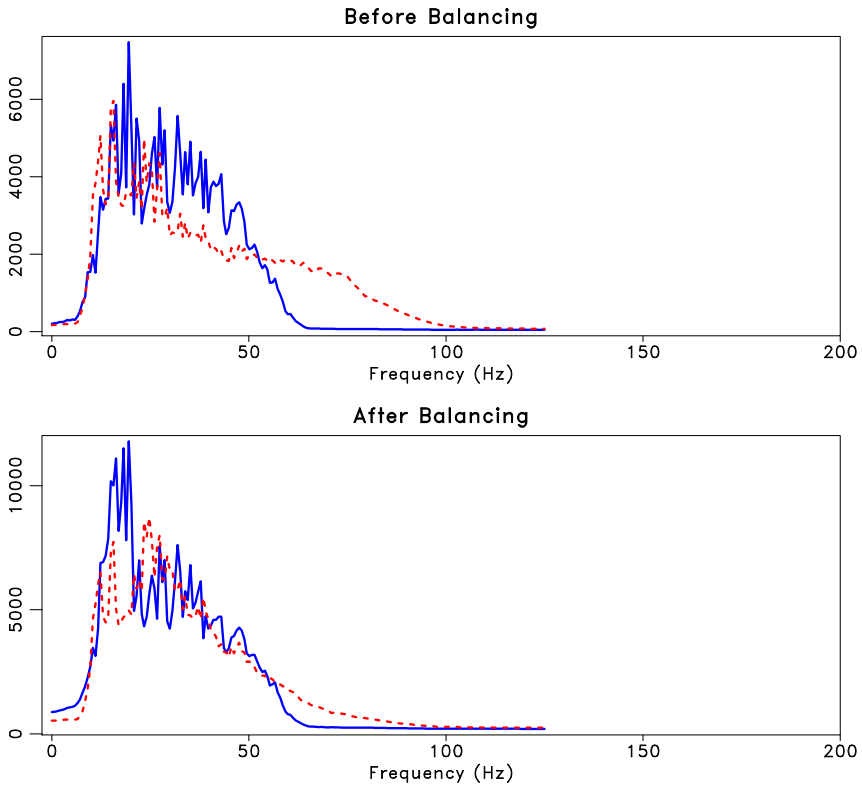

Figure 4.5: PP trace spectrum is plotted in solid line, and PS trace spectrum is plotted in dash line. Spectral balancing helps compensate the amplitude and spectral differences between them. chapter4/registration apa-sp-1

Local Correlation and γ Scan

Fomel (2007a) defines local seismic attributes as seismic attributes that measure seismic signal characteristics not instantaneously at each signal point and not globally across a data window but locally in the neighborhood of each point. Shaping regularization has been used to control the locality and smoothness of local attributes. The idea of locality extends from local frequency to other attributes, such as the correlation coefficient between two different data sets. Measuring and maximizing correlation between PP and PS waves helps improve PP and PS image registration. A similar approach has been adopted by Leiceaga et al. (2010) in their alignment technique for PS and PP data. They modified one data set from a PP and PS pair by a constrained mathematical transformation such that the cross-correlation between the two data sets is maximized.

A global correlation coefficient is commonly used to measure the similarity between two data sets. Statistically, if X and Y are two random variables, the global correlation coefficient is defined as

$$\gamma_{x,y} = \frac{E[(X-\mu_X)(Y-\mu_Y)]}{\sigma_X \sigma_Y} \ , \tag{4.6}$$

where E is expected value operator, μ_X and μ_Y are expected values of X and Y, σ_X and σ_Y are standard deviations of X and Y. The correlation coefficient can be estimated by sample correlation coefficient $\gamma_{x,y}$

$$\gamma_{x,y} = \frac{\sum_{i=1}^{n}(x_i-\bar{x})(y_i-\bar{y})}{\sqrt{\sum_{i=1}^{n}(x_i-\bar{x})^2 \sum_{i=1}^{n}(y_i-\bar{y})^2}} \ , \tag{4.7}$$

where $\bar{x} = \frac{1}{n}\sum_{i=1}^{n} x_i$ and $\bar{y} = \frac{1}{n}\sum_{i=1}^{n} y_i$.

Assuming $a_i = x_i - \bar{x}$ and $b_i = y_i - \bar{y}$, the correlation coefficient can be represented as a

product of two least squares inverse Fomel (2007a)

$$\gamma^2 = \gamma_1\gamma_2 \;, \tag{4.8}$$

$$\gamma_1 = (\mathbf{a}^T\mathbf{a})^{-1}(\mathbf{a}^T\mathbf{b}) \;, \tag{4.9}$$

$$\gamma_2 = (\mathbf{b}^T\mathbf{b})^{-1}(\mathbf{b}^T\mathbf{a}) \;, \tag{4.10}$$

where $\mathbf{a}$ and $\mathbf{b}$ are vector notations of a_i and b_i. Then, let $\mathbf{A}$ be a diagonal operator composed from the elements of $\mathbf{a}$ and $\mathbf{B}$ be a diagonal operator composed from the elements of $\mathbf{b}$. Localizing equations 4.9 and 4.10 amounts to adding regularization to inversion (Fomel, 2007b). Using shaping regularization, scalar γ_1 and γ_2 turn into vectors $\mathbf{c_1}$ and $\mathbf{c_2}$

$$\mathbf{c_1} = [\lambda^2\mathbf{I} + \mathbf{S}(\mathbf{A}^T\mathbf{A} - \lambda^2\mathbf{I})]^{-1}\mathbf{S}\mathbf{A}^T\mathbf{b} \;, \tag{4.11}$$

$$\mathbf{c_2} = [\lambda^2\mathbf{I} + \mathbf{S}(\mathbf{B}^T\mathbf{B} - \lambda^2\mathbf{I})]^{-1}\mathbf{S}\mathbf{B}^T\mathbf{a} \;. \tag{4.12}$$

Fomel (2007a) defined a local similarity measure by applying the componentwise product of vectors.

The problem of cycle skips and erroneous local minima in the registration objective function is another major difficulty in accurate automatic registration. To solve such problems, Fomel and Backus (2003) developed an algorithm for rapid scanning of the field for possible registration. The residual γ_0 parameter corresponds to the warping function. Hence, by scanning γ_0, we shall be able to measure the local similarity of PP and PS images. If γ_0 equals one, that means no additional streching or sequeezing is needed; if γ_0 is greater than one, squeezing is required. Scanning γ_0 and

$$w(x,t) = w_0[x, \gamma_0(x,t)t] \;, \tag{4.13}$$

where $w_0(x,t)$ is the initial time warping function, and $\gamma_0(x,t)$ is the function picked through the residual γ scan. It is important to discriminate γ_0 from V_p/V_s ratio γ. As we can see in Figure 4.6(a), γ_0 value is greater than one, which means squeezing is needed in this case. After I applied warp function, γ_0 value converge to one in Figure 4.6(b).

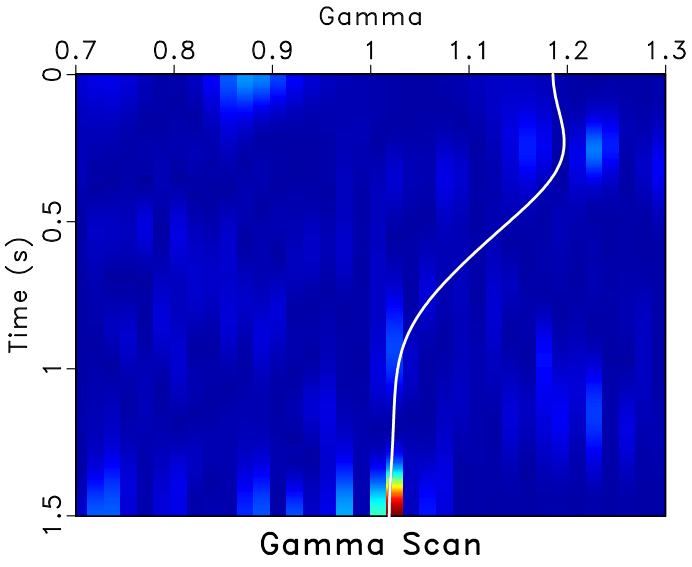

(a)

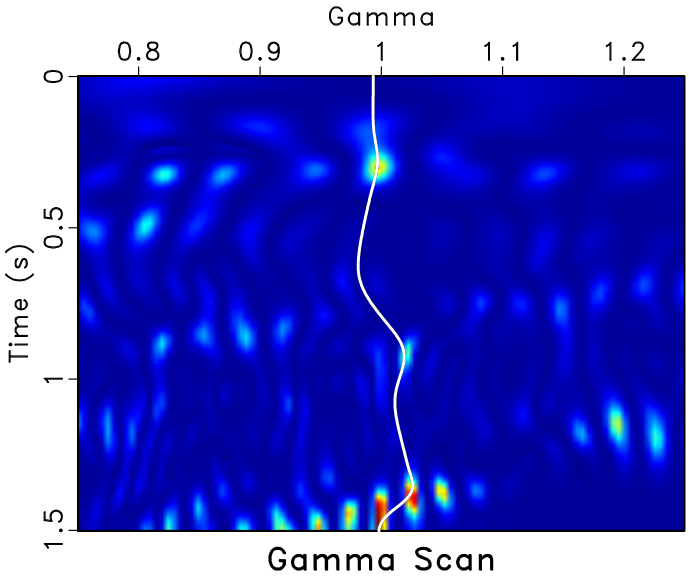

(b)

Figure 4.6: The smooth registration trend has been picked after the first iteration (a) and the second iteration (b). The trend picked in (b) shows after the second iteration the correlation converges to one better. chapter4/registration apat-scn-0,apat-scn-1

Final Registration Tuning

After picking the residual trend, the time warping function is updated by using shaping regularization. I then apply a least-squares optimization algorithm (Fomel and Backus, 2003) to improve the final result. The objective of registration states is to minimize the difference between PP and a warped PS image, that is

$$\min_{a,w} \sum_t \|P(t) - a(t)C[w(t)]\|_2^2 \ . \tag{4.14}$$

The Gauss-Newton algorithm has been applied. It is a modification of Newtons method for minimization developed for the particular case when the objective function can be written as a sum of squares. Because the amplitude gain $a(t)$ term appears linearly, the problem is separable and allows for an effective variable projection technique (Kaufman, 1975). In general, a separable problem states as (Björck, 1996)

$$\min_{\mathbf{a},\mathbf{w}} \|e(\mathbf{a},\, \mathbf{w})\|_2 \,, \quad \begin{pmatrix} \mathbf{a} \\ \mathbf{w} \end{pmatrix} \begin{matrix} \} p \\ \} q \end{matrix} \ , \quad p + q = k \ . \tag{4.15}$$

Figure **??** shows the final result is improved. We find the seismic events in the warped PS image registered at the same time depth as the corresponding events in PP image. The events at about 0.25 second and 1.4 seconds in the warped PS image matches their counterparts in the PP image. To justify and validate the method and result, we interleave traces from spectrally balanced PP and PS images in Figure 4.9. As can be seen, after registration, the warped PS session matches PP session better.

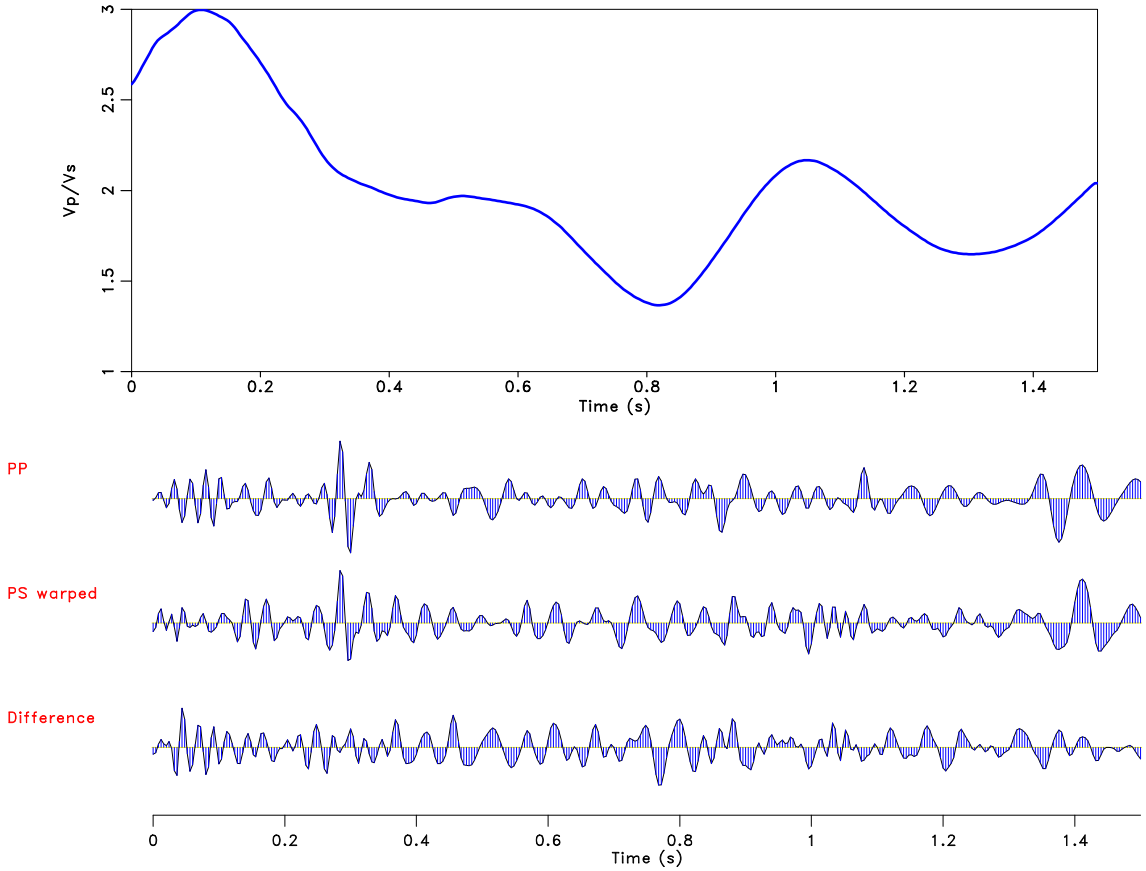

Figure 4.7: After registration, the warped PS trace matches the PP trace. The difference between these two traces is smaller compared to the result in initial registration. chapter4/registration apat-psw-11

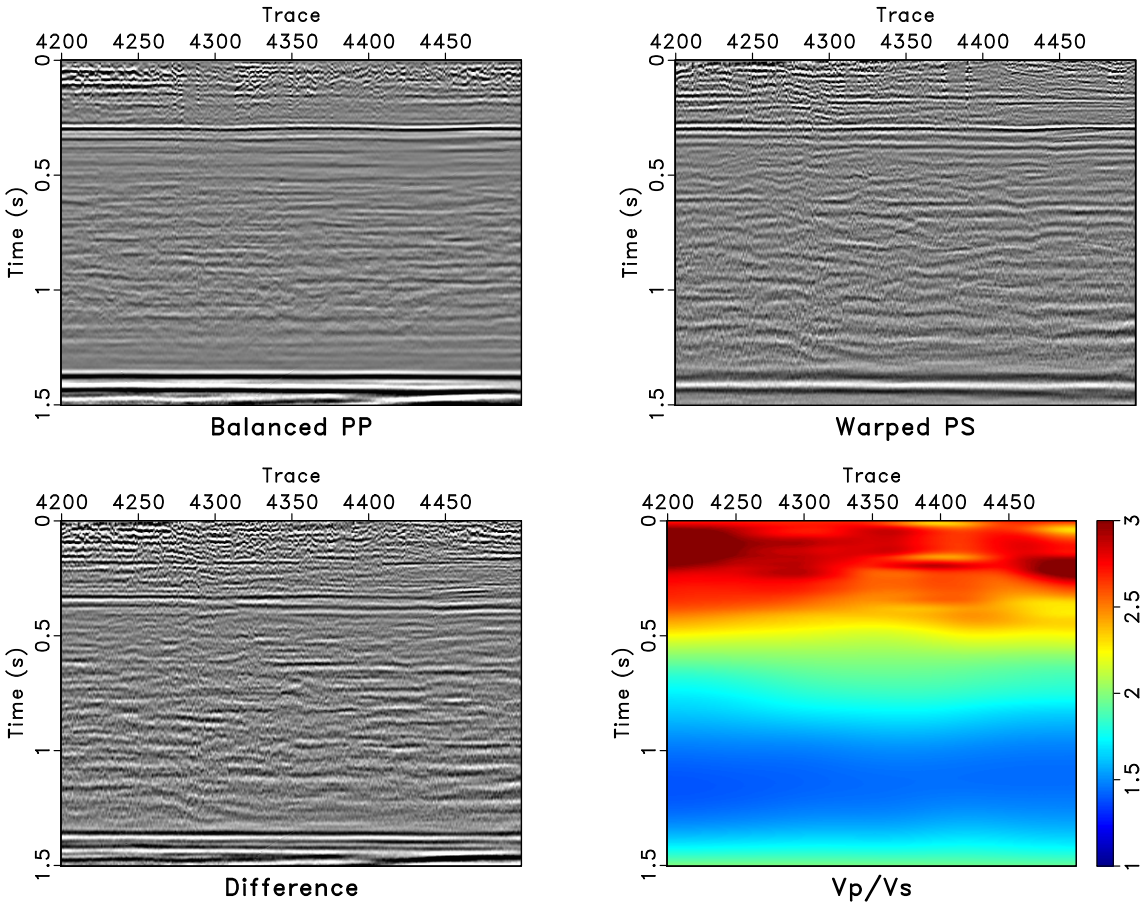

Figure 4.8: Result of image registration. chapter4/registration apa-psw-12

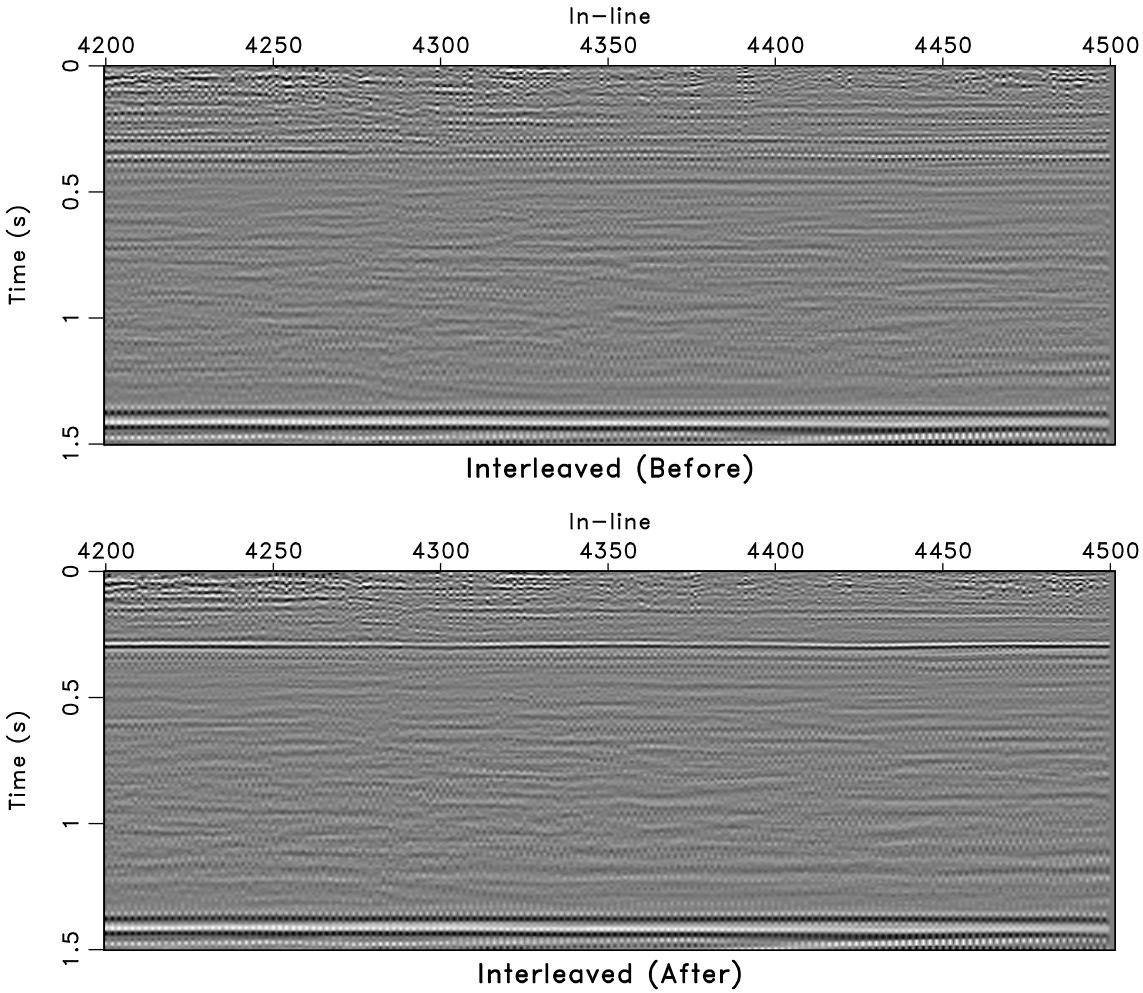

Figure 4.9: PP and warped PS sessions interleaved before (a) and after (b) final registration. The seismic event at about 0.25 second is well displayed in (b) after final registration. chapter4/registration apa-in0-01

Chapter 5

Conclusions

Summary

Spectral recomposition models the spectral components of seismic traces. It can be used to extract the most significant components of seismic data, and helps the interpreter to reveal various depositional systems in seismic volumes. The same technique can also be used in forward modeling as well to provide detailed information about different layers in the subsurface. I analyzed and modeled frequency components of multicomponent seismic data by using spectral recomposition. With the help of local time-frequency analysis, I recomposed the spectra of a seismic trace at different time depths. The technique of spectral recomposition has been used to model the frequency components of PP and PS data, which provides another dimension for interpretation. It provides information related to any specific layer the user might be interested in and provides a deeper understanding of seismic attenuation in the subsurface.

Spectral recomposition can also be used to estimate thin-bed thickness and search for tuning frequency and provides a robust and phase-independent approach to seismic thickness estimation. Compared with conventional methods involving adjacent peaks and troughs peaking, spectral recomposition requires simply peak frequency and amplitude estimation. To apply separable, nonlinear, least-squares estimation for spectral recomposition, interpreters and processors may need to decide how many components to fit into the model.

The multistep image registration approach helps provide solid results for interpretation.

In a given stratigraphic interval of the geologic section, registration correlates the P- and S-wave profiles to determine t_s/t_p ratio, which is equivalent to V_p/V_s for a vertical propagation path. Using a multistep approach, the registration process no longer depends on sonic logs or VSP data. That is, interpreters can simply use multicomponent data to do registration. The relatively independent result can then be used in joint interpretation with geological factors. Moreover, the multistep approach provides us V_p/V_s ratio as a by-product. I applied the multistep approach on the field data. As a result, the warped PS image matches the PP image reasonably well.

Appendix

C code

```
/*
  Copyright (C) 2012 University of Texas at Austin

  This program is free software; you can redistribute it and/or modify
  it under the terms of the GNU General Public License as published by
  the Free Software Foundation; either version 2 of the License, or
  (at your option) any later version.

  This program is distributed in the hope that it will be useful,
  but WITHOUT ANY WARRANTY; without even the implied warranty of
  MERCHANTABILITY or FITNESS FOR A PARTICULAR PURPOSE.  See the
  GNU General Public License for more details.

  You should have received a copy of the GNU General Public License
  along with this program; if not, write to the Free Software
  Foundation, Inc., 59 Temple Place, Suite 330, Boston,
  MA  02111-1307  USA
*/

#include <float.h>
#include <math.h>
#include <rsf.h>
#include <stdio.h>
#include "gaussel.h"

int main(int argc, char* argv[])
{
//r: ricker spectrum; rp: partial of ricker spectrum
//m: peak frequency; a: spectral amplitude
    int n2, na, ia, i, j, niter, k, iter, n, l, ib;
    float eps, f, f0, f2, df;
    float *m0=NULL, *a, *m, *m2, *m3, *e, *ap;
    float *data, *dataout, **rt, **r, **rs, **rp, **rpt;
    float *rtd, **rptr, **rtrp, *ra, *gamma, **rk, *rka, *rptd, *rkd;
    float **rpa, **rap, **raprpa, **raprpat, **mt, *gt, *dm, *est, r2, rss;
    bool verb;
    sf_file in, out, ma1, ma2;

    sf_init (argc,argv);
    in  = sf_input("in");
    out = sf_output("out");
    ma1 = sf_output("ma1");
    ma2 = sf_output("ma2");
```

```
if (SF_FLOAT != sf_gettype(in)) sf_error("Need float input");
if (!sf_histint(in,"n1",&na)) sf_error("No n1= in input");
n2 = sf_leftsize(in,1);

if (!sf_histfloat(in,"d1",&df)) sf_error("No d1= in input");
if (!sf_histfloat(in,"o1",&f0)) sf_error("No o1= in input");
/*user needs to decide*/
/*number of terms*/
if (sf_getint("n",&n) && !sf_getfloats("m",m0,n)) {
    m0 = sf_floatalloc(n);
    for (i=0; i<n; i++) {
        m0[i] = f0+0.4/n*(i+1)*(na-1)*df;
    }
}
else
{
    sf_error("n is not specified.");
}
for (i=0; i<n; i++) {
    sf_warning("i=%d m0=%g f0=%g", i, m0[i], f0);
}

if (!sf_getint("niter",&niter)) niter=100;
if (!sf_getbool("verb",&verb)) verb=false;

sf_putint(ma1,"n1",n);
sf_putint(ma1,"nf",na);
sf_putfloat(ma1,"df",df);
sf_putfloat(ma1,"f0",f0);
sf_fileflush(ma1,in);

sf_putint(ma2,"n1",n);
sf_putint(ma2,"nf",na);
sf_putfloat(ma2,"df",df);
sf_putfloat(ma2,"f0",f0);
sf_fileflush(ma2,in);


data = sf_floatalloc(na);
eps = 10.*FLT_EPSILON;
eps *= eps;

for (i=0; i < n2; i++) {
    sf_warning("slice %d of %d;",i+1,n2);
```

```
/*read in data*/
sf_floatread(data,na,in);

m = sf_floatalloc(n);

for (j = 0; j < n; j++) {
    m[j] = m0[j];
}

m2 = sf_floatalloc(n);
m3 = sf_floatalloc(n);
e = sf_floatalloc(n);
a = sf_floatalloc(n);
r = sf_floatalloc2(n,na);
rp = sf_floatalloc2(n,na);
rt = sf_floatalloc2(na,n);
rpt = sf_floatalloc2(na,n);
rtd = sf_floatalloc(n);
rptd = sf_floatalloc(n);
rs = sf_floatalloc2(n,n);
rptr = sf_floatalloc2(n,n);
rtrp = sf_floatalloc2(n,n);
rk = sf_floatalloc2(n,n);
rka = sf_floatalloc(n);
rptd = sf_floatalloc(n);
rkd = sf_floatalloc(n);
raprpa = sf_floatalloc2(n,na);
rpa = sf_floatalloc2(n,na);
rap = sf_floatalloc2(n,na);
ap = sf_floatalloc(n);
gamma = sf_floatalloc(na);
ra = sf_floatalloc(na);
raprpat = sf_floatalloc2(na,n);
dm = sf_floatalloc(n);
est = sf_floatalloc(na);
mt = sf_floatalloc2(n,n);

for (k=0;k<n;k++) {
    m[k] = m0[k];
}

for (iter = 0; iter < niter; iter++) {
    for (k = 0; k < n; k++) {
        m2[k] = m[k]*m[k];
        m3[k] = m2[k]*m[k];
```

```
        rtd[k] = 0.;
        rptd[k] = 0.;
        for (ia = 0; ia < na; ia++) {
            f = f0 + ia*df;
            f2 = f*f;
            e[k] = exp(-f2/m2[k]);
            rt[k][ia] = e[k]*f2/m2[k];
            rpt[k][ia] = 2.*e[k]*f2*(f2-m2[k])/(m3[k]*m2[k]);
            rtd[k] += rt[k][ia]*data[ia];
            rptd[k] += rpt[k][ia]*data[ia];
        }
    }

    for (ib = 0; ib < na; ib++) {
        for (l = 0; l < n; l++) {
            r[ib][l] = rt[l][ib];
            rp[ib][l] = rpt[l][ib];
        }
    }

    for (k = 0; k < n; k++) {
        for (l = 0; l < n; l++) {
            rs[k][l] = 0.;
            for (ib = 0; ib < na; ib++) {
                rs[k][l] += rt[k][ib]*r[ib][l];
            }
        }
    }

    for (l = 0; l < n; l++) {
        for (k = 0; k < n; k++) {
            rptr[l][k] = 0.;
            rtrp[l][k] = 0.;
            for (ib = 0; ib < na; ib++) {
                rptr[l][k] += rpt[l][ib]*r[ib][k];
                rtrp[l][k] += rt[l][ib]*rp[ib][k];
            }
        }
    }

    for (k = 0; k < n; k++) {
        for (l = 0; l < n; l++) {
            if (k == l) {
                rs[k][l] = rs[k][l]+eps;
            }
```

```
            }
        }

        gaussel_init(n);
        gaussel_solve(rs, rtd, a);

        for (k = 0; k < n; k++) {
            for (l = 1; l < n; l++) {
                rk[k][l] = rptr[k][l]+rtrp[k][l];
            }
        }

        for (k = 0; k < n; k++) {
            rka[k] = 0;
            for (l = 0; l < n; l++) {
                rka[k] += rk[k][l]*a[l];
            }
        }

        for (k = 0; k < n ; k++) {
            rptd[k] = 0;
            for (ib = 0; ib < na; ib++) {
                rptd[k] += rpt[k][ib]*data[ib];
            }
        }

        for (k = 0; k < n; k++) {
            rkd[k] = rptd[k]-rka[k];
        }

        gaussel_init(n);
        gaussel_solve(rs, rkd, ap);

/*aprarp is X; gamma is Y*/

        for (ib = 0; ib < na; ib++) {
            f = f0 + ib*df;
            f2 = f*f;
            ra[ib] = 0;
            for (k = 0; k < n; k++) {
                ra[ib] += a[k]*exp(-f2/m2[k])*f2/m2[k];
            }
        }

        for (ib = 0; ib < na; ib++) {
```

```
            gamma[ib] = data[ib]-ra[ib];
        }

        for (ib = 0; ib < na; ib++) {
            for (k = 0; k < n; k++) {
                rpa[ib][k] = rp[ib][k]*a[k];
            }
        }

        for (ib = 0; ib < na; ib++) {
            for (k = 0; k < n; k++) {
                rap[ib][k] = r[ib][k]*ap[k];
            }
        }

        for (ib = 0; ib < na; ib++) {
            for (k = 0; k < n; k++) {
                raprpa[ib][k] = rap[ib][k] + rpa[ib][k];
            }
        }

        for (k = 0; k < n; k++) {
            for (ib = 0; ib < na ; ib++) {
                raprpat[k][ib] = raprpa[ib][k];
            }
        }

// least squares for delta m.
        for (k = 0; k < n; k++) {
            for (l = 0; l < n; l++) {
                mt[k][l] = 0;
                for (ib = 0; ib < na; ib++) {
                    mt[k][l] += raprpat[k][ib]*raprpa[ib][l];
                }
            }
        }

        gt = sf_floatalloc(n);
        for (k = 0; k < n; k++) {
            gt[k] = 0;
            for (ib = 0; ib < na; ib++) {
                gt[k] += raprpat[k][ib]*gamma[ib];
            }
        }
        gaussel_init(n);
```

```
        gaussel_solve(mt, gt, dm);

        r2 = 0;
        for (ib = 0; ib < na; ib++) {
            f = f0 + ib*df;
            f2 = f*f;
            est[ib] = 0;
            for (k = 0; k < n; k++) {
                est[ib] += a[k]*exp(-f2/m2[k])*f2/m2[k];
            }
            r2 += (est[ib]-data[ib])*(est[ib]-data[ib]);
        }

        if (verb && 5000 > n2) sf_warning("iter=%d r2=%g", iter, r2);

        if (r2 < eps ) break;

        for (k = 0; k < n; k++) {
            m[k] += dm[k];
        }
    }
    for (k = 0; k < n; k++) {
        m[k] = fabsf(m[k]);
        m2[k] = m[k]*m[k];
    }

    sf_floatwrite(m2,n,ma1);

    sf_floatwrite(a,n,ma2);

    rss = 0;
    dataout = sf_floatalloc(na);
    for (ib = 0; ib < na; ib++) {
        f = f0 + ib*df;
        f2 = f*f;
        dataout[ib] = 0;
        for (k = 0; k < n; k++) {
            dataout[ib] += a[k]*exp(-f2/m2[k])*f2/m2[k];
        }
        rss += (data[ib]-dataout[ib])*(data[ib]-dataout[ib]);
    }

    for (k = 0; k < n; k++) {
        sf_warning("m=%g a=%g",m[k],a[k]*m[k]*sqrtf(SF_PI)*0.5);
    }
```

```
        sf_warning("Residual sum of squares equals %g",rss);

        sf_floatwrite(dataout,na,out);
    }

    sf_warning(".");

    exit (0);
}
```

Madagascar script

```
from rsf.proj import *
import math

par = {
    'nt':1000, 'dt':0.004,'ot':0,    'lt':'t','ut':'s',
    'kt':100,    # wavelet delay
    }
# peak frequencies
freqs = (10,20,50)

# number of components
nc = len(freqs)

# generate wavelet
for c in range(nc):
    par['f'] = freqs[c]
    wave = 'wave%d' % c
    Flow(wave,None,
         '''
         spike nsp=1 mag=1 n1=%(nt)d d1=%(dt)g o1=%(ot)g
         k1=%(kt)d |
         ricker1 frequency=%(f)g | scale axis=123 |
         put label1=t label2=x label3=y | transp
         ''' % par)
    Plot(wave,
         '''
         window |
         window n1=200 |
         graph title="Ricker Wavelet of %(f)g Hz"
         plotfat=6 label1="t" label2= unit2= font=2
         labelsz=10 titlesz=16 labelfat=2 titlefat=4
         wantaxis2=n
         ''' % par)
```

```
Flow('waves','wave0 wave1 wave2','add ${SOURCES[1:%d]}' % nc)
Plot('waves',
     '''
     window | window n1=200 |
     wiggle poly=y title="Wavelet with %g, %g and %g Hz
     Ricker Component"
     pclip=100
     plotfat=6 plotcol=7 label1="Time" label2="Amplitude"
     unit2= font=2
     labelsz=10 titlesz=16 titlefat=4 labelfat=2
     min2=-0.5 max2=1
     ''' % freqs)
Flow('spec0','waves','transp | spectra')
Plot('spec0',
     '''
     graph labelsz=10 titlesz=16 wanttitle=n plotcol=7
     plotfat=5
     label1="Frequency" unit1="Hz" label2="Amplitude" unit2=
     min1=0 max1=120 min2=0 max2=0.5 labelfat=2 font=2
     ''')
# spectral recomposition
Flow('ricker0 ma1 ma2', 'spec0',
     '''
     rickerfit n=%d verb=y
     ma1=${TARGETS[1]} ma2=${TARGETS[2]}
     ''' % nc)
Plot('ricker0',
     '''
     graph symbol=o labelsz=10 titlesz=16 symbolsz=10
     plotfat=12 plotcol=2
     title="Wavelet Spectrum and Its Estimation"
     label2="" label1="" unit2= unit1=
     min1=0 max1=120 min2=0 max2=0.5 font=2
     titlefat=4 labelfat=2
     ''')
Plot('spectrum', 'ricker0 spec0', 'Overlay')

for c in range(nc):
    comp = 'comp%d' % c
    freq = 'freq%d' % c
    ampl = 'ampl%d' % c
    Flow(freq,'ma1',
         '''
         window n1=1 f1=%d | spray axis=1 n=501 d=0.25 o=0
         ''' % c)
```

```
    Flow(ampl,'ma2',
         '''
         window n1=1 f1=%d | spray axis=1 n=501 d=0.25 o=0
         ''' % (c))
    Flow(comp,[freq,ampl],
         '''
         math m2=${SOURCES[0]} a=${SOURCES[1]}
         output="a*exp(-x1*x1/m2)*x1*x1/m2"
         ''')
    Flow('c'+comp,comp,'rtoc')
    dcmp = 'dcmp%d' % c
    Flow(dcmp,['waves','c'+comp],
         '''
         window | fft1 |
         math c=${SOURCES[1]} output="c*exp(I*arg(input))"
         | fft1 inv=y
         ''')
    Plot(dcmp,
         '''
         window |
         window n1=200 |
         graph title="Ricker Wavelet" plotfat=6 label1="t"
         label2= unit2= font=2
         labelsz=10 titlesz=16 labelfat=2 titlefat=4
         wanttitle=n wantaxis2=n
         symbol=o plotcol=5 symbolsz=10
         ''')
    Plot(comp,
         '''
         window |
         window n1=480 |
         graph title="Ricker Wavelet Spectrum" plotfat=6
         label1="Frequency" unit1=Hz label2= unit2= font=2
         labelsz=10 titlesz=16 labelfat=2 titlefat=4
         wanttitle=y
         min1=0 min2=0 max1=120 max2=0.5
         ''')

Plot('rkspec','comp0 comp1 comp2','Overlay')

Result('rk','waves spectrum rkspec','OverUnderAniso')

Plot('rk0','wave0 dcmp0','Overlay')
Plot('rk1','wave1 dcmp1','Overlay')
Plot('rk2','wave2 dcmp2','Overlay')
```

```
Result('rickers','rk0 rk1 rk2','SideBySideAniso')

End()
```

Bibliography

Aki, K., and P. G. Richards, 2009, Quantitative Seismology, Second Edition: University Science Books.

Backus, M., P. Murray, B. Hardage, and R. Graebner, 2006a, High-resolution multicomponent seismic imaging of deepwater gas-hydrate systems: The Leading Edge, **25**, 578–584.

Backus, M. M., B. A. Hardage, and R. J. Graebner, 2006b, High-resolution multicomponent seismic imaging of deepwater gas-hydrate systems: The Leading Edge, **25**, 578–596.

Björck, Å., 1996, Numerical Methods for Least Squares Problems: Society for industrial and applied mathematics.

Browaeys, T. J., and S. Fomel, 2009, Fractal heterogeneities in sonic logs and low-frequency scattering attenuation: Geophysics, **74**, WA77–WA92.

Cai, Y., S. Fomel, and H. Zeng, 2012, Spectral recomposition using separable nonlinear least squares: Expanded Abstracts 82^{nd} SEG International Convention, Submitted.

Caldwell, J., 1999, Marine multicomponent seismology: The Leading Edge, 1274–1282.

Cary, P., 2001, Multicomponent seismic exploration in Canada-one person's perspective: The Recorder, **September**, 62–67.

Castagna, J. P., S. Sun, and R. W. Siegfried, 2003, Instantaneous spectral analysis: Detection of low-frequency shadows associated with hydrocarbons: The Leading Edge, **22**, 120–127.

Chakraborty, A., and D. Okaya, 1995, Frequency-time decomposition of seismic data using wavelet-based methods: Geophysics, **60**, 1906–1916.

Chen, G., G. Matteucci, B. Fahmy, and C. Finn, 2008, Spectral-decomposition response to reservoir

fluids from a deepwater west africa reservoir: Geophysics, **73**, C23–C30.

Chopra, S., and K. Marfurt, 2007, Seismic Attributes for Prospect Identification and Reservoir Characterization: Society of Exploration Geophysicists.

Chung, W. Y., and D. Corrigan, 1985, Gathering modeconverted shear waves: A model study: Expanded Abstracts 55^{th} SEG International Convention, 602–604.

Claerbout, J. F., 1975, Spectral balancing: SEP report, **1**, 172–181.

Danbom, S. H., and S. N. Domenico, 1987, Shear-wave Exploration: Soc. of Expl. Geophys.

DeAngelo, M., M. Backus, B. Hardage, and P. Murray, 2003, Depth registration of p-wave and c-wave seismic data for shallow marine sediment characterization, Gulf of Mexico: The Leading Edge, **22**, 96–105.

Dilay, A., and J. Eastwood, 1995, Spectral analysis applied to seismic monitoring of thermal recovering: The Leading Edge, **14**, 1117–1122.

Fomel, S., 2007a, Local seismic attributes: Geophysics, **72**, A29–A33.

———, 2007b, Shaping regularization in geophysical estimation: Geophysics, **72**, R29–R36.

Fomel, S., and M. Backus, 2003, Multicomponent seismic data registration by least squares: Expanded Abstracts 73^{rd} SEG International Convention, 781–784.

Fomel, S., M. Backus, K. Fouad, and B. Hardage, 2005, A multistep approach to multicomponent seismic image registration with application to a west texas carbonate reservoir study: Expanded Abstracts 75^{th} SEG International Convention, 1018–1021.

Gaiser, J. E., 1999, Applications of vector coordinate systems of 3-d converted-wave data: The Leading Edge, 1290–1300.

Gaiser, J. E., E. Loinger, H. Lynn, and . Vetri, 2001, *ps*-wave birefringence analysis at the Emilio field for fracture characterization: 63^{rd} EAGE Conf. and Tech. Exhibit. Extended Abstract, N 07.

Galloway, W. E., P. E. Ganey-Curry, X. Li, and R. T. Buffler, 2000, Cenozoic depositional history of the Gulf of Mexico Basin: AAPG Bulletin, **84**, 1743–1774.

Garotta, R., P.-Y. Granger, and H. Dariu, 2002, Combined interpretation of pp and ps data provides direct access to elastic rock properties: The Leading Edge, **21**, 532–535.

Golub, G. H., and V. Pereyra, 1973, The differentiation of pseudo-inverses and nonlinear least squares problems whose variables separate: Numerical Analysis, **10**, 413–432.

Grechka, V., and I. Tsvankin, 2002, $pp + ps = ss$: Geophysics, **67**, 1961–1971.

Hardage, B., M. DeAngelo, P. Murray, and D. Sava, 2011, Mulicomponent Seismic Technology: Society of exploration geophysicists.

Hirsche, K., D. Hampson, D. Peron, and B. Russell, 2005, Simultaneous inversion of pp and ps seismic data a case history from western canada: , A10.

Horton, C. W., 1943, Secondary arrivals in a well velocity survey: Geophysics, **8**, 290–296.

Kaufman, L., 1975, Variable projection methods for solving separable nonliner least squares problems: BIT, **14**, 156–166.

Leiceaga, G. G., J. Silva, F. Artola, E. Marquez, and J. Vanzeler, 2010, Enhanced density estimation from prestack inversion of multicomponent seismic data: The Leading Edge, **29**, 1220–1226.

Li, X. Y., 1998, Fracture detection using $p - p$ and $p - s$ waves in multicomponent sea-floor data: Expanded Abstracts 68^{th} SEG International Convention, 2056–2059.

Li, Y., X. Zheng, and Y. Zhang, 2011, High-frequency anomalies in carbonate reservoir characterization using spectral decomposition: Geophysics, **76**, V47–V57.

Liner, C. L., and R. G. Clapp, 2004, Nonlinear pairwise alignment of seismic traces: Geophysics, **69**, P1552–1559.

Liu, G., S. Fomel, and X. Chen, 2011, Time-frequency analysis of seismic data using local attributes:

Geophysics, **76**, P23–P34.

Liu, J., 2006, Spectral Decomposition and Its Application in Mapping Stratigraphy and Hydrocarbons: PhD thesis, Univeristy of Houston.

McGookey, D. P., 1975, Gulf coast cenozoic sediments and structures: An excellent example of extra-continental sedimentation: Gulf Coast Association of Geologic Societies Transactions, **25**, 104–120.

Meier, M. A., and P. J. Lee, 2009, Converted-wave resolution: Geophysics, **74**, Q1–Q16.

Modersitzki, J., 2004, Numerical Methods for Image Registration: Oxford University Press.

Nickel, M., and L. Sonneland, 2004, Automated ps to pp event registration and estimation of a high-resolution vp-vs ratio volume: Expanded Abstracts 74^{th} SEG International Convention, 869–872.

Osborne, M. R., 2007, Separable least squares, variable projection, and the Gauss-Newton algorithm: Electronic Transactions on Numerical Analysis, **28**, 1–15.

Partyka, G. J., J. Gridley, and J. Lopez, 1999, Interpretational applications of spectral decomposition in reservior characterization: The Leading Edge, **18**, 353–360.

Rodriguez, C., 2000, Advanced Marine Methods: Ocean-bottom and Vertical Cable Analyses: PhD thesis, University of Calgary.

Scolnik, H. D., 1972, On the Solution of Non-linear Least Squares Problems: , IFIP Congress, 1258–1265.

Sheriff, R., 2002, Encyclopedic Dictionary of Applied Geophysics: Soc. of Expl. Geophys.

Simmons, J., and M. Backus, 2001, Shear waves from 3-d-9-c seismic reflection data: The Leading Edge, 604–612.

Stewart, R., J. Gaiser, R. Brown, and D. Lawton, 2002, Converted-wave seismic exploration: Methods: Geophysics, **67**, P1348–1363.

———, 2003, Converted-wave seismic exploration: Application: Geophysics, **68**, P40–57.

Tatham, R., M. D. McCormack, and E. B. Neitzel, 1991, Multicomponent Seismology in Petroleum Exploration: Soc. of Expl. Geophys.

Tessmer, G., and A. Behle, 1988, Common reflection point data-stacking: Geophysical Prospecting, **36**, 671–688.

Tomasso, M., R. Bouroullec, and D. R. Pyles, 2010, The use of spectral recomposition in tailored forward seismic modeling of outcrop analogs: AAPG Bulletin, **94**, 457–474.

Tsvankin, I., and V. Grechka, 2011, Seismology of Azimuthally Anisotropy Media and Seismic Fracture Charaterization: Soc. of Expl. Geophys.

van Dok, R. R., J. E. Gaiser, and J. E. Markert, 2001, Processing and analysis of ps-wave data from a 3d/3c land survey for fracture characterization: 63^{rd} EAGE Conf. and Tech. Exhibit. Extended Abstract, P 117.

Wolberg, G., 1990, Digital Image Warping: IEEE Computer Society.

Yilmaz, O., 2001, Seismic Data Analysis: Soc. of Expl. Geophys.

Zeng, H., and M. M. Backus, 2005a, Interpretive advantages of 90-phase wavelets: Part 1modeling: Geophysics, **70**, C7C15.

———, 2005b, Interpretive advantages of 90-phase wavelets: Part 2seismic applications: Geophysics, **70**, C17C24.

Zeng, H., and T. F. Hentz, 2004, High-frequency sequence stratigraphy from seismic sedimentology: Applied to miocene, vermilion block 50, tiger shoal area, offshore louisiana: AAPG Bulletin, **88**, 153–174.

Zhu, X., S. Altan, and J. Li, 1999, Recent advances in multicomponent processing: The Leading Edge, 1283–1288.

Zitová, B., and J. Flusser, 2003, Image registration methods: a survey: Image and Vision Computing, **21**, 977–1000.